

Flexible Readout and Unconditional Reset for Superconducting Multi-Qubit Processors with Tunable Purcell Filters

Yong-Xi Xiao,^{1,2,*} Da'er Feng,^{1,2,*} Xu-Yang Gu,^{1,2} Gui-Han Liang,^{1,2} Ming-Chuan Wang,^{1,2} Zheng-Yu Peng,^{1,2} Bing-Jie Chen,^{1,2} Yu Yan,^{1,2} Zheng-Yang Mei,^{1,2} Si-Lu Zhao,^{1,2} Yi-Zhou Bu,^{1,2} Cheng-Lin Deng,^{1,2} Xiaohui Song,^{1,2} Dongning Zheng,^{1,2,3,4} Yu-Xiang Zhang,^{1,2} Yun-Hao Shi,¹ Zhongcheng Xiang,^{1,2,3,4,†} Kai Xu,^{1,2,3,4,5,‡} and Heng Fan^{1,2,3,4,5,§}

¹*Beijing National Laboratory for Condensed Matter Physics,
Institute of Physics, Chinese Academy of Sciences, Beijing 100190, China*

²*School of Physics, University of Chinese Academy of Sciences Beijing 100049, China*

³*Beijing Academy of Quantum Information Sciences, 100193 Beijing, China*

⁴*Hefei National Laboratory, 230088 Hefei, China*

⁵*Songshan Lake Materials Laboratory, 523808 Dongguan, Guangdong, China*

Qubit readout and reset are critical components for the practical realization of quantum computing systems, as outlined by the DiVincenzo criteria. Here, we present a scalable architecture employing frequency-tunable nonlinear Purcell filters designed specifically for superconducting qubits. This architecture enables flexible readout and unconditional reset functionalities. Our readout protocol dynamically adjusts the effective linewidth of the readout resonator through a tunable filter, optimizing the signal-to-noise ratio during measurement while suppressing photon noise during idle periods. Achieving a readout fidelity of 99.3% without using Josephson parametric amplifiers or traveling-wave parametric amplifiers, even with a small dispersive shift, demonstrates its effectiveness. For reset operations, our protocol utilizes the tunable coupler adjacent to the target qubit as an intermediary to channel qubit excitations into the Purcell filter, enabling rapid dissipation. We demonstrate unconditional reset of both leakage-induced $|2\rangle$ and $|1\rangle$ states within 200 ns (error rate $\leq 1\%$), and reset of the $|1\rangle$ state alone in just 75 ns. Repeated reset cycles (≤ 600 ns) further reduce the error rate below 0.1%. Furthermore, the filter suppresses both photon noise and the Purcell effect, thereby reducing qubit decoherence. This scalable Purcell filter architecture shows exceptional performance in qubit readout, reset, and protection, marking it as a promising hardware component for advancing fault-tolerant quantum computing systems.

Qubit readout and reset are two essential DiVincenzo criteria for practical quantum computing systems [1]. Superconducting qubits have emerged as a leading platform for scalable fault-tolerant quantum computation due to breakthroughs in coherence times, integration, and control fidelity [2–4]. Recent advances have enabled large-scale quantum information tasks, including quantum simulation and error correction [5–9]. However, the growing complexity of these applications demands simultaneous improvements in high-fidelity readout and rapid, low-error qubit reset. These challenges are critical to addressing decoherence, leakage errors, and scalability in superconducting processors [10–34].

Balancing high readout fidelity with qubit protection remains a central challenge in dispersive readout of superconducting qubits [10–14]. While fixed-frequency linear Purcell filters improve signal-to-noise ratio (SNR) and suppress the Purcell effect [12–17, 35], they cannot fully mitigate photon-noise-induced dephasing. Recent demonstrations of nonlinear Purcell filters on single-qubit devices [22] have enabled photon-noise-tolerant readout but rely on large dispersive shifts and remain unverified for scalability. Meanwhile, prior multi-qubit implementations of high-fidelity readout typically depend on Josephson parametric amplifiers (JPAs) or traveling-wave parametric amplifiers (TWPAs) to achieve sub-1% readout error [24, 25].

In this Letter, we present a scalable architecture of frequency-tunable nonlinear Purcell filters integrated into a superconducting multi-qubit processor. By dynamically adjusting the effective linewidth of readout resonators through filter tuning, we optimize SNR for qubit state discrimination while suppressing photon noise during idle periods. Critically, this approach achieves 99.3% readout fidelity without requiring JPAs or TWPAs, surpassing prior multi-qubit benchmarks under comparable conditions. Our design operates with a small dispersive shift, enabling compatibility with compact, low-noise architectures.

Additionally, to demonstrate the functional versatility of our tunable Purcell filter, we experimentally implement a coupler-assisted qubit reset protocol that utilizes the filter as a dedicated dissipation channel. This method achieves unconditional reset of leakage-induced $|2\rangle$ and $|1\rangle$ within 200 ns (error rate $\leq 1\%$), while reset of $|1\rangle$ alone completes in just 75 ns. Repeated reset cycles (≤ 600 ns total) further reduce the error rate to $\leq 0.1\%$. Compared to existing schemes that utilize readout resonators for dissipation [28, 36], our approach significantly shortens reset times and minimizes crosstalk in multi-qubit systems.

Our experiment employs a flip-chip superconducting quantum processor, interconnected via indium bump bonding. The device consists of aluminum-based copla-

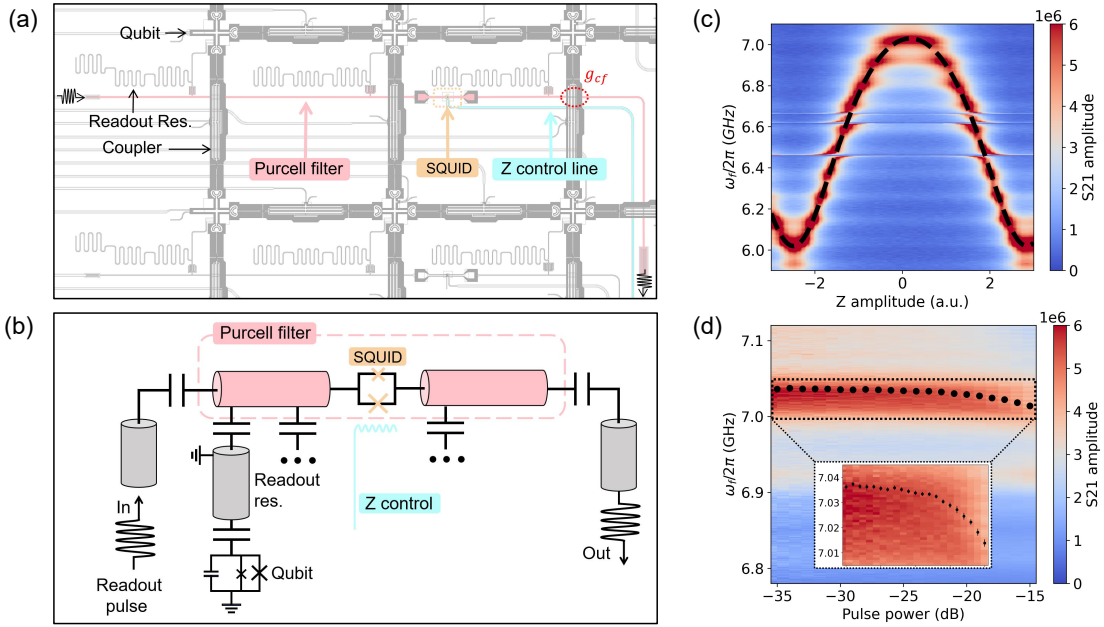


FIG. 1. Tunable Purcell filter integrated in a flip-chip quantum processor. (a) Filter-related structure. The filter (pink) consists of a half-wavelength resonator with open-ended capacitance coupling to the transmission line. The midpoint of filter is integrated with a SQUID (orange) containing two Josephson junctions, of which the flux is modulated by the Z control line (blue). Each filter is shared by three readout resonators for qubit readout and coupled with couplers (circled in red) for qubit reset. (b) Distributed-element circuit model of the relevant device section with color coding matching (a). The ellipses denote other resonator-qubit systems and couplers capacitively coupled to the filter. (c) The variation of S21 amplitude under different Z amplitude applied to the SQUID. Black dashed curve indicates fitted resonance frequencies of filter passbands. (d) Power-dependent Kerr nonlinearity effect on the filter passband frequency. Black markers represent fitted resonance frequencies at the passband peaks.

nar waveguide circuits fabricated on sapphire substrates. The top chip contains 24 qubits, 38 couplers, and 8 Superconducting Quantum Interference Devices (SQUIDs) dedicated to filters, while the bottom chip serves as the wiring layer housing readout resonators, the main bodies of filters, and associated transmission lines. As shown in Fig. 1(a) and (b), each tunable Purcell filter is parametrically coupled to three readout resonators via capacitance. A filter comprises a nonlinear structure, based on a $\lambda/2$ cavity with open ends capacitively coupled with transmission-line, incorporating a SQUID (composed of two Josephson junctions in parallel) at its midpoint. Note that the Josephson junctions of a filter are located on the top layer and are connected to the geometric cavity on the bottom layer through indium bumps. This design offers the advantage of enabling simultaneous fabrication of the Josephson junctions of filters, qubits, and couplers, thereby simplifying the fabrication process. Inputting DC signals through the Z-control line generates flux bias to tune the filter frequency among 6.02 GHz to 7.06 GHz (Fig. 1(c)). The power-dependent Kerr nonlinearity effect is another reason for frequency changes. The nonlinear frequency shift remains negligible at low power levels (Fig. 1(d)) because of a small anharmonic-

ity of $\alpha_f/2\pi = 4.47$ MHz. The frequency of this filter can be dynamically tuned through SQUID Z amplitude and readout pulse amplitude. This enables real-time optimization of effective linewidth κ_{eff} of readout resonators through the filter, aiming to achieve optimal readout conditions (typically targeting $2\chi = \kappa_{\text{eff}}$ where 2χ is the dispersive shift). This addresses the limitation of fixed-bandwidth linear filters, where fabrication-induced frequency deviations may cause $2\chi \neq \kappa_{\text{eff}}$. And the tunable filter passband frequency expands the frequency allocation range of readout resonators on a single feedline, thereby mitigating frequency crowding in multi-qubit readout.

The SNR represents a crucial metric in high fidelity dispersive readout [20, 23], scaling with $\text{SNR}^2 \propto \eta\kappa\bar{n}|\sin(2\theta)|^2t$, with $|\sin(2\theta)| = \chi\kappa/(\chi^2 + \kappa^2/4)$, where κ denotes the linewidth of the readout resonator, η is the quantum efficiency, \bar{n} is the average photon number, and t is the readout time. $|\sin(2\theta)|^2 = 1$ is satisfied when $\kappa = 2\chi$. Figure 2(a) illustrates the readout scheme incorporating a tunable filter, of which the role manifests in modifying κ_{eff} to optimize SNR. Filter frequency modulation induces corresponding changes in κ_{eff} , as shown in Fig. 2(b). The measurement-induced dephasing rate

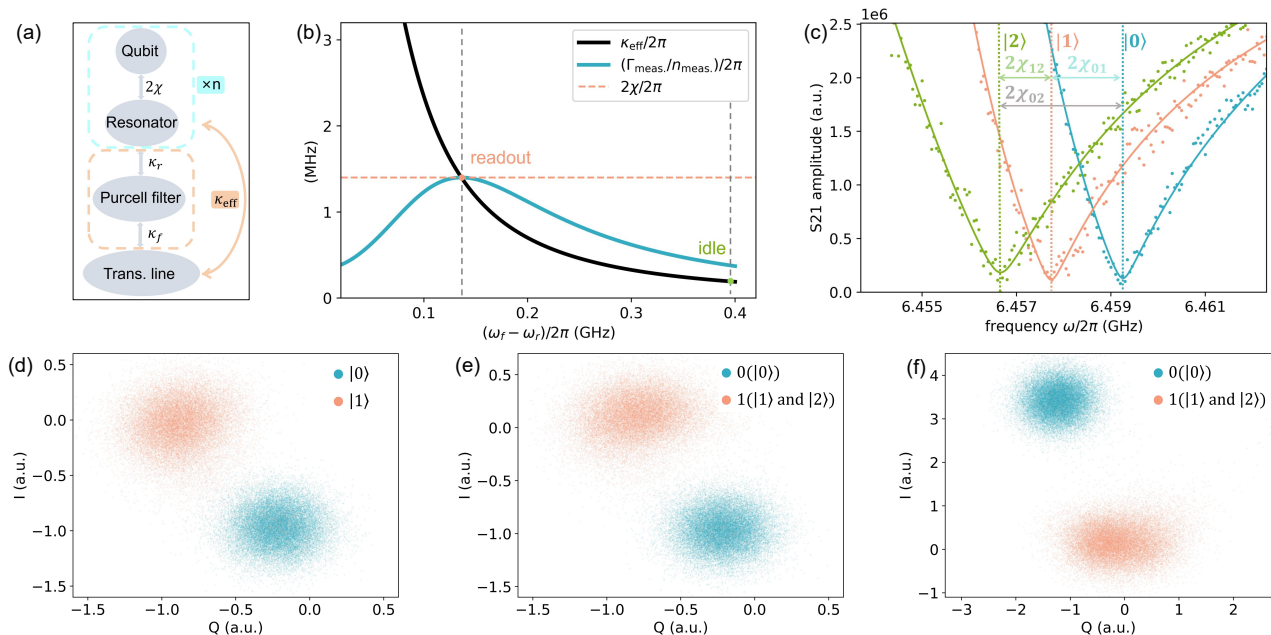


FIG. 2. Experimental demonstration of flexible readout. (a) Schematic of the qubit readout system with tunable Purcell filters. The tunable Purcell filter functions to adjust κ_{eff} . Each filter is coupled with n resonators ($n=3$ here). (b) Variation curves of κ_{eff} and $\Gamma_{\text{meas.}}/n_{\text{meas.}}$ versus frequency difference between the filter and readout resonator. The filter frequency resides at a point maximizing $\Gamma_{\text{meas.}}/n_{\text{meas.}}$ (where $\kappa_{\text{eff}} = 2\chi$) during readout, while at a lower point during idle time. (c) The fitted dressed-state frequencies of the readout resonator with different qubit states. To maximize state distinguishability when distinguishing qubit states $|i\rangle$ and $|j\rangle$, the effective linewidth is set to $\kappa_{\text{eff}} = 2\chi_{ij}$. (d-f) Typical data of IQ raw data: (d) 500 ns readout with direct measurement. (e) 500 ns readout with pre- π_{12} -pulse, mitigating qubit decoherence effects compared to (d). (f) 1077 ns readout duration with pre- π_{12} -pulse, achieving enhanced SNR over (e) and 99.3% readout fidelity.

$\Gamma_{\text{meas.}}$ is defined by $\Gamma_{\text{meas.}}/n_{\text{meas.}} = 2\chi|\sin(2\theta)|$, where $n_{\text{meas.}}$ is the average photon number in readout resonator. And $\Gamma_{\text{meas.}}$ is the upper limit of measurement rate [37]. During active readout operations, the filter frequency aligns with the $\kappa_{\text{eff}} = 2\chi$ configuration to maximize SNR and $\Gamma_{\text{meas.}}/n_{\text{meas.}}$ with a given 2χ . During idle periods, the filter frequency remains at a low-dephasing-rate operating point (idle point, where $\kappa \neq 2\chi$), enabling enhanced suppression of photon noise compared to conventional fixed-frequency filters. To verify the tunable filter's suppression effect on photon noise, we intentionally inject Gaussian white noise into the readout transmission line and measure the dephasing rate of a qubit, as shown in Fig. 3. Furthermore, the idle point maintains greater detuning between filter and qubit, providing additional suppression of Purcell effects.

Notably, the dispersive shift 2χ of dressed states under different qubit states is not a fixed parameter (Fig. 2(c)). This observation highlights important considerations: while direct measurements of qubit $|0\rangle$ - $|1\rangle$ remain standard practice, contemporary protocols also employ π_{12} -pulse-assisted $|0\rangle$ - $|2\rangle$ readout [19, 38]. $|0\rangle$ - $|2\rangle$ readout means implementing a non-discriminating readout between $|1\rangle$ and $|2\rangle$ states, wherein: (i) All results measured in either $|1\rangle$ or $|2\rangle$ are registered as logical '1'. (ii)

Only $|0\rangle$ measurements yield logical '0' outputs. The logical '0' or '1' is the single-shot measurement result. The tunable filter provides adaptable κ_{eff} values to accommodate various readout requirements. For instance, Figs. 2(d) and (e) present IQ raw data for $|0\rangle$ - $|1\rangle$ and $|0\rangle$ - $|2\rangle$ readouts with 500 ns integration times, achieving SNR of 4.6 and 4.9 respectively. The $|0\rangle$ - $|2\rangle$ readout mitigates T_1 -limited fidelity constraints, enabling extension of integration time to 1077 ns (Fig. 2(f)) with SNR improvement to 6.4 and a readout fidelity $\geq 99.3\%$. Here readout fidelity is defined as: $F = (P(0|0) + P(1|1))/2$, where $P(a|b)$ denotes the probability that qubit is prepared in $|b\rangle$ state and then measured in $|a\rangle$ state. And SNR is calculated with $\text{SNR} = 2|m_0 - m_1|/(\sigma_0 + \sigma_1)$ [17, 20], where $m_{0(1)}$ and $\sigma_{0(1)}$ are the mean and standard deviation of the Gaussian fits to IQ data of $|0\rangle$ ($|1\rangle$). Notably, the extended readout duration originates from the weak coupling design between readout resonators and qubits, implemented to preserve qubit coherence for complex multi-qubit gate operations. Each IQ distribution derives from 30,000 single-shot measurements.

Furthermore, we introduce a coupler-assisted qubit reset protocol leveraging the Purcell filter as a dissipation channel. Rapid qubit reset techniques could be applied to various quantum information processing tasks espe-

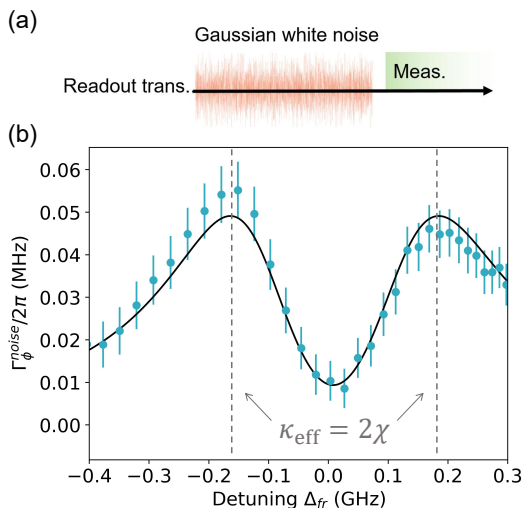


FIG. 3. Evaluation of the noise tolerance. (a) Pulse sequence. The qubit T_2 is measured while applying Gaussian white noise through the readout transmission line. (b) Qubit dephasing rate versus detuning. The dephasing rate $\Gamma_{\text{meas.}}$ reaches a maximum when the detuning Δ_{fr} satisfies $\kappa_{\text{eff}} = 2\chi$. The black curve shows the fit using a photon-noise-induced dephasing model (see Supplemental Material for details).

cially the quantum error correction codes [39]. Reset protocols are categorized into active (conditional) [40, 41] and passive (unconditional) [26–28] approaches based on whether qubit state information is required. While introducing additional decay channels risks complicating multi-qubit integration, the coupler-assisted reset offers a hardware-efficient solution [28, 36]. However, existing schemes utilize the readout resonator for dissipation, whose rate is significantly lower than that of the filter. Employing the filter would further reduce the reset time and the error rate. In a flip-chip processor, qubits and couplers are typically placed on one layer, while transmission lines and Purcell filters are located on another layer [3, 5, 9]. Inevitably, filters traverse above couplers or qubits as shown in fig. 1(a). The former results in a coupling strength g_{cf} between filters and couplers. We ingeniously exploit this coupling to facilitate qubit reset. Crucially, the filter and readout resonators remain detuned throughout the process (filter: 7.0 GHz, readout resonators: 6.4–6.6 GHz in this experiment), effectively suppressing photon leakage into the readout resonators. This detuning strategy requires a frequency-tunable filter, as fixed-frequency filters must operate near the readout resonator frequency to maintain measurement fidelity. And the detuning avoid keeping the coupler at the readout resonator frequency, which would trigger complex multi-body processes.

As illustrated in Fig. 4(a), our reset protocol comprises three sequential steps. Step 1 involves adiabatic state swap between the qubit and coupler. The reso-

nance between the coupler and the target qubit introduces non-zero coupling between the target qubit and another qubit connected via the same coupler. To ensure exclusive photon transfer to the coupler, the frequencies of these two qubits are intentionally detuned by 800 MHz here. Step 2 utilizes the capacitive coupling mentioned above to perform adiabatic swap between the coupler and the filter. Step 3 involves rapid photon dissipation from the filter, enabled by its leakage rate (linewidth) $\kappa_f/2\pi = 150$ MHz. It is noted that the linewidth of the filter is approximately 100 times larger than that of the readout resonator. Thus step 3 executes concurrently within operational timeframe of Step 2, requiring virtually no additional time. Especially, the coupler frequency starts below the target qubit frequency (and above the neighboring), sweeps through it, and continues ascending to the filter frequency to suppress Landau-Zener-Stückelberg interference [42], which could otherwise degrade reset fidelity.

To validate the unconditional nature and leakage-error mitigation capability of this reset protocol, we conduct the experimental demonstration outlined in Fig. 4(b). First, the qubit is prepared in varying excited states by applying π_{01} pulses and π_{12} fractional pulses of different amplitudes ($A\pi_{12}$ with A from 0 to 1). Then a standardized reset operation (waveform details are shown in Supplemental Material) is executed by adjusting the coupler flux bias. State preparation is repeated for m rounds. After each round, reset operations would be executed for n cycles. The result of a preparation round with $\pi_{01} + A\pi_{12}$ and a reset cycle is shown in Fig. 4(c). The qubit-coupler swap and coupler-filter swap are completed within 30 ns and 170 ns, respectively, yielding a total reset within 200 ns. Immediate post-reset qubit measurements reveal the population of excited state below 1.2% across all initial states. After accounting for a 0.45% ground-state readout error (attributed to state discrimination limitation and natural thermal excitation), the unconditional reset error per cycle is inferred to below 1%.

Further investigation of consecutive multi-cycle reset operations after a round of state preparation with $\pi_{01} + \pi_{12}$, as shown in Fig. 4(d), demonstrates progressive reduction of residual excitations with increasing reset cycles, converging to natural thermal excitation levels (quantified by a deviation less than 0.1% from ground-state readout error line) after three cycles (600 ns). Critically, multiple reset cycles do not accumulate errors via photon recapture, confirming effective dissipation through the filter. Consider the following scenario: the qubit state is repeatedly prepared m rounds with an interval of 1 microsecond, and the cycles of resets after each state preparation is $n = 3$. As shown in Fig. 4(d), the residual thermal excitation does not increase with the growth of m , which indicates that short-time multiple excitations and resets of the qubit is supported. In other words, this dissipation channel can be rapidly reused.

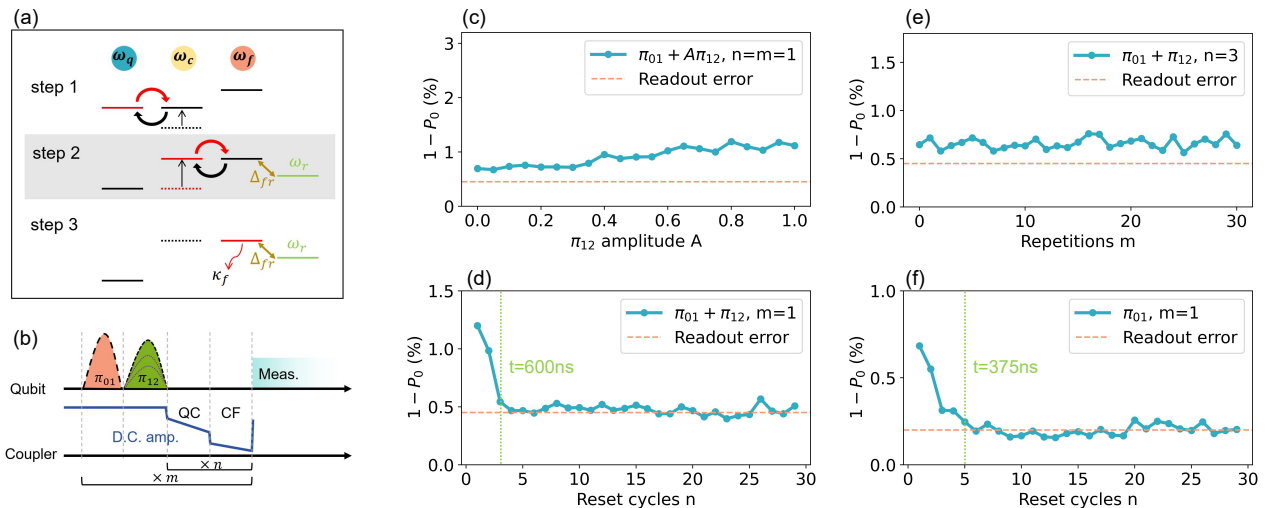


FIG. 4. Experimental demonstration of unconditional qubit reset. (a) Reset protocol. Step 1: Qubit-coupler (QC) swap. Step 2: Coupler-filter (CF) swap. Step 3: Dissipation of excitation into the environment via the Purcell filter. Steps 2 and 3 occur concurrently, with the filter detuned from the readout resonators to avoid crosstalk. (b) Pulse sequence for state preparation, reset, and measurement. (c-f) Residual qubit excitation after reset, quantified by the measured $|0\rangle$ state population P_0 . (c) Single reset cycle (200 ns), preparing initial state with π_{01} and $A\pi_{12}$, where $0 \leq A \leq 1$. (d) Multiple reset cycles, with state preparation using π_{01} and π_{12} . (e) Repeated state preparation (for m rounds) followed by three reset cycles each time. (f) Multiple reset cycles with initialization using only the full π_{01} pulse.

When exclusively considering $|1\rangle$ excitation, we employ square pulse for QC and CF swap. The single-cycle reset operation can be optimized to complete within 75 ns (4.5 ns/ 70 ns for qubit-coupler/coupler-filter swap) with a error rate below 1%. And the residual thermal excitation decreases and converges to the natural scenario after the 5-th cycle (375 ns), with a deviation from readout error line below 0.1%. Each data point in Fig. 4(c-f) is derived from 30,000 repetitions of single-shot measurements. The readout error line in Fig. 4(f) differs from those in other figures dues to different readout parameters. Comparing with recent reports on the unconditional reset for quantum error correction [36, 39, 43], the time cost and error rate of our protocol are smaller. Therefore, our reset protocol has the potential to be applied in complex algorithms such as quantum error correction, where the reset operations are executed frequently.

In conclusion, we present a scalable structure of tunable-frequency nonlinear Purcell filters for superconducting multi-qubit processors. Based on this structure, we implement a flexible readout protocol featuring the κ_{eff} -tuning capability of filters to maximize SNR during readout and suppress photon noise during idle time. Without employing JPA or TWPA, we achieve 99.3% readout fidelity with a small dispersive shift of 1.4 MHz. By leveraging the coupling between couplers and filters in a flip-chip architecture, we propose an unconditional qubit reset protocol. This protocol eliminates both leakage-induced $|2\rangle$ and $|1\rangle$ states with a rate exceeds natural qubit relaxation by a factor of 10^3 . Thus, this

tunable-frequency nonlinear Purcell filter structure represents a highly potential auxiliary hardware component to advance the development of fault-tolerant quantum computing systems. Future improvements may focus on extending the filter geometry by utilizing the frequency-tunable property in a $n\lambda/2$ resonator to readout more qubits. Since the reset time is primarily limited by the coupler-filter coupling strength g_{cf} , increasing g_{cf} could achieve faster reset operation.

We acknowledge the support from the Synergetic Extreme Condition User Facility (SECUF). This work is supported by the National Natural Science Foundation of China (Grants Nos. T2121001, 92265207, T2322030, 12122504, 12274142, 92365206, 12104055), the Innovation Program for Quantum Science and Technology (Grant No. 2021ZD0301800), the Beijing Nova Program (No. 20220484121), and the China Postdoctoral Science Foundation (Grant No. GZB20240815).

* These authors contributed equally to this work.

† zcxiaang@iphy.ac.cn

‡ kaixu@iphy.ac.cn

§ hfan@iphy.ac.cn

- [1] D. DiVincenzo, The physical implementation of quantum computation, *Fortschritte der Physik* **48**, 771 (2000).
- [2] C. Wang, X. Li, H. Xu, Z. Li, J. Wang, Z. Yang, Z. Mi, X. Liang, T. Su, C. Yang, G. Wang, W. Wang, Y. Li, M. Chen, C. Li, K. Linghu, J. Han, Y. Zhang, Y. Feng,

- Y. Song, T. Ma, J. Zhang, R. Wang, P. Zhao, W. Liu, G. Xue, Y. Jin, and H. Yu, Towards practical quantum computers: transmon qubit with a lifetime approaching 0.5 milliseconds, *npj Quantum Inf.* **8**, 3 (2022).
- [3] P. Zhang, Y. Gao, X. Xu, N. Wang, H. Dong, C. Guo, J. Deng, X. Zhang, J. Chen, S. Xu, K. Wang, Y. Wu, C. Zhang, F. Jin, X. Zhu, A. Zhang, Y. Zou, Z. Tan, Z. Cui, Z. Zhu, F. Shen, T. Li, J. Zhong, Z. Bao, L. Zhao, J. Hao, H. Li, Z. Wang, C. Song, Q. Guo, H. Wang, and D. Poletti, Emergence of steady quantum transport in a superconducting processor, *Nat. Commun.* **15**, 10115 (2024).
- [4] G.-H. Liang, X.-H. Song, C.-L. Deng, X.-Y. Gu, Y. Yan, Z.-Y. Mei, S.-L. Zhao, Y.-Z. Bu, Y.-X. Xiao, Y.-H. Yu, M.-C. Wang, T. Liu, Y.-H. Shi, H. Zhang, X. Li, L. Li, J.-Z. Wang, Y. Tian, S.-P. Zhao, K. Xu, H. Fan, Z.-C. Xiang, and D.-N. Zheng, Tunable-coupling architectures with capacitively connecting pads for large-scale superconducting multiqubit processors, *Phys. Rev. Appl.* **20**, 044028 (2023).
- [5] Y. Zhao, Y. Ye, H.-L. Huang, Y. Zhang, D. Wu, H. Guan, Q. Zhu, Z. Wei, T. He, S. Cao, F. Chen, T.-H. Chung, H. Deng, D. Fan, M. Gong, C. Guo, S. Guo, L. Han, N. Li, S. Li, Y. Li, F. Liang, J. Lin, H. Qian, H. Rong, H. Su, L. Sun, S. Wang, Y. Wu, Y. Xu, C. Ying, J. Yu, C. Zha, K. Zhang, Y.-H. Huo, C.-Y. Lu, C.-Z. Peng, X. Zhu, and J.-W. Pan, Realization of an Error-Correcting Surface Code with Superconducting Qubits, *Phys. Rev. Lett.* **129**, 030501 (2022).
- [6] S. Krinner, N. Lacroix, A. Remm, A. Di Paolo, E. Genois, C. Leroux, C. Hellings, S. Lazar, F. Swiadek, J. Herrmann, G. J. Norris, C. K. Andersen, M. Mueller, A. Blais, C. Eichler, and A. Wallraff, Realizing repeated quantum error correction in a distance-three surface code, *Nature* **605**, 669 (2022).
- [7] C.-L. Deng, Y. Liu, Y.-R. Zhang, X.-G. Li, T. Liu, C.-T. Chen, T. Liu, C.-W. Lu, Y.-Y. Wang, T.-M. Li, C.-P. Fang, S.-Y. Zhou, J.-C. Song, Y.-S. Xu, Y. He, Z.-H. Liu, K.-X. Huang, Z.-C. Xiang, J.-C. Wang, D.-N. Zheng, G.-M. Xue, K. Xu, H. F. Yu, and H. Fan, High-Order Topological Pumping on a Superconducting Quantum Processor, *Phys. Rev. Lett.* **133**, 140402 (2024).
- [8] Y.-Y. Wang, Y.-H. Shi, Z.-H. Sun, C.-T. Chen, Z.-A. Wang, K. Zhao, H.-T. Liu, W.-G. Ma, Z. Wang, H. Li, J.-C. Zhang, Y. Liu, C.-L. Deng, T.-M. Li, Y. He, Z.-H. Liu, Z.-Y. Peng, X. Song, G. Xue, H. Yu, K. Huang, Z. Xiang, D. Zheng, K. Xu, and H. Fan, Exploring Hilbert-Space Fragmentation on a Superconducting Processor, *PRX Quantum* **6**, 010325 (2025).
- [9] G. Q. AI and Collaborators, Quantum error correction below the surface code threshold, *Nature* **638**, 920 (2025).
- [10] A. Blais, R.-S. Huang, A. Wallraff, S. M. Girvin, and R. J. Schoelkopf, Cavity quantum electrodynamics for superconducting electrical circuits: An architecture for quantum computation, *Phys. Rev. A* **69**, 062320 (2004).
- [11] J. Koch, T. M. Yu, J. Gambetta, A. A. Houck, D. I. Schuster, J. Majer, A. Blais, M. H. Devoret, S. M. Girvin, and R. J. Schoelkopf, Charge-insensitive qubit design derived from the Cooper pair box, *Phys. Rev. A* **76**, 042319 (2007).
- [12] E. Jeffrey, D. Sank, J. Y. Mutus, T. C. White, J. Kelly, R. Barends, Y. Chen, Z. Chen, B. Chiaro, A. Dunsworth, A. Megrant, P. J. J. O'Malley, C. Neill, P. Roushan, A. Vainsencher, J. Wenner, A. N. Cleland, and J. M. Martinis, Fast Accurate State Measurement with Superconducting Qubits, *Phys. Rev. Lett.* **112**, 190504 (2014).
- [13] T. Walter, P. Kurpiers, S. Gasparinetti, P. Magnard, A. Potočnik, Y. Salathé, M. Pechal, M. Mondal, M. Oppliger, C. Eichler, and A. Wallraff, Rapid High-Fidelity Single-Shot Dispersive Readout of Superconducting Qubits, *Phys. Rev. Appl.* **7**, 054020 (2017).
- [14] J. Heinsoo, C. K. Andersen, A. Remm, S. Krinner, T. Walter, Y. Salathé, S. Gasparinetti, J.-C. Besse, A. Potočnik, A. Wallraff, and C. Eichler, Rapid High-fidelity Multiplexed Readout of Superconducting Qubits, *Phys. Rev. Appl.* **10**, 034040 (2018).
- [15] D. Sank, Z. Chen, M. Khezri, J. Kelly, R. Barends, B. Campbell, Y. Chen, B. Chiaro, A. Dunsworth, A. Fowler, E. Jeffrey, E. Lucero, A. Megrant, J. Mutus, M. Neeley, C. Neill, P. J. J. O'Malley, C. Quintana, P. Roushan, A. Vainsencher, T. White, J. Wenner, A. N. Korotkov, and J. M. Martinis, Measurement-Induced State Transitions in a Superconducting Qubit: Beyond the Rotating Wave Approximation, *Phys. Rev. Lett.* **117**, 190503 (2016).
- [16] M. Khezri, A. Opremcak, Z. Chen, K. C. Miao, M. McEwen, A. Bengtsson, T. White, O. Naaman, D. Sank, A. N. Korotkov, Y. Chen, and V. Smelyanskiy, Measurement-induced state transitions in a superconducting qubit: Within the rotating-wave approximation, *Phys. Rev. Appl.* **20**, 054008 (2023).
- [17] P. A. Spring, L. Milanovic, Y. Sunada, S. Wang, A. F. van Loo, S. Tamate, and Y. Nakamura, Fast Multiplexed Superconducting-Qubit Readout with Intrinsic Purcell Filtering Using a Multiconductor Transmission Line, *PRX Quantum* **6**, 020345 (2025).
- [18] D. Egger, M. Werninghaus, M. Ganzhorn, G. Salis, A. Fuhrer, P. Müller, and S. Filipp, Pulsed Reset Protocol for Fixed-Frequency Superconducting Qubits, *Phys. Rev. Appl.* **10**, 044030 (2018).
- [19] S. S. Elder, C. S. Wang, P. Reinhold, C. T. Hann, K. S. Chou, B. J. Lester, S. Rosenblum, L. Frunzio, L. Jiang, and R. J. Schoelkopf, High-Fidelity Measurement of Qubits Encoded in Multilevel Superconducting Circuits, *Phys. Rev. X* **10**, 011001 (2020).
- [20] A. Blais, A. L. Grimsmo, S. M. Girvin, and A. Wallraff, Circuit quantum electrodynamics, *Rev. Mod. Phys.* **93**, 025005 (2021).
- [21] R. Shillito, A. Petrescu, J. Cohen, J. Beall, M. Hauru, M. Ganahl, A. G. Lewis, G. Vidal, and A. Blais, Dynamics of Transmon Ionization, *Phys. Rev. Appl.* **18**, 034031 (2022).
- [22] Y. Sunada, K. Yuki, Z. Wang, T. Miyamura, J. Ilves, K. Matsuura, P. A. Spring, S. Tamate, S. Kono, and Y. Nakamura, Photon-Noise-Tolerant Dispersive Readout of a Superconducting Qubit Using a Nonlinear Purcell Filter, *PRX Quantum* **5**, 010307 (2024).
- [23] Y. Ye, J. B. Kline, S. Chen, A. Yen, and K. P. O'Brien, Ultrafast superconducting qubit readout with the qurton coupler, *Sci. Adv.* **10**, eado9094 (2024).
- [24] F. m. c. Swiadek, R. Shillito, P. Magnard, A. Remm, C. Hellings, N. Lacroix, Q. Ficheux, D. C. Zanuz, G. J. Norris, A. Blais, S. Krinner, and A. Wallraff, Enhancing Dispersive Readout of Superconducting Qubits through Dynamic Control of the Dispersive Shift: Experiment and Theory, *PRX Quantum* **5**, 040326 (2024).
- [25] A. Bengtsson, A. Opremcak, M. Khezri, D. Sank,

- A. Bourassa, K. J. Satzinger, S. Hong, C. Erickson, B. J. Lester, K. C. Miao, A. N. Korotkov, J. Kelly, Z. Chen, and P. V. Klimov, Model-Based Optimization of Superconducting Qubit Readout, *Phys. Rev. Lett.* **132**, 100603 (2024).
- [26] Y. Zhou, Z. Zhang, Z. Yin, S. Huai, X. Gu, X. Xu, J. Allcock, F. Liu, G. Xi, Q. Yu, H. Zhang, M. Zhang, H. Li, X. Song, Z. Wang, D. Zheng, S. An, Y. Zheng, and S. Zhang, Rapid and unconditional parametric reset protocol for tunable superconducting qubits, *Nat. Commun.* **12**, 5924 (2021).
- [27] P. Magnard, P. Kurpiers, B. Royer, T. Walter, J.-C. Besse, S. Gasparinetti, M. Pechal, J. Heinsoo, S. Storz, A. Blais, and A. Wallraff, Fast and Unconditional All-Microwave Reset of a Superconducting Qubit, *Phys. Rev. Lett.* **121**, 060502 (2018).
- [28] L. Chen, S. P. Fors, Z. Yan, A. Ali, T. Abad, A. Osman, E. Moschandreou, B. Lienhard, S. Kosen, H.-X. Li, D. Shiri, T. Liu, S. Hill, A.-A. Amin, R. Rehammar, M. Dahiya, A. Nylander, M. Rommel, A. F. Roudsari, M. Caputo, G. Leif, J. Govenius, M. Dobšicek, M. F. Giannelli, A. F. Kockum, J. Bylander, and G. Tancredi, Fast unconditional reset and leakage reduction in fixed-frequency transmon qubits (2024), [arXiv:2409.16748 \[quant-ph\]](https://arxiv.org/abs/2409.16748).
- [29] Y. Sunada, S. Kono, J. Ilves, S. Tamate, T. Sugiyama, Y. Tabuchi, and Y. Nakamura, Fast Readout and Reset of a Superconducting Qubit Coupled to a Resonator with an Intrinsic Purcell Filter, *Phys. Rev. Appl.* **17**, 044016 (2022).
- [30] T. Yoshioka, H. Mukai, A. Tomonaga, S. Takada, Y. Okazaki, N.-H. Kaneko, S. Nakamura, and J.-S. Tsai, Active initialization experiment of a superconducting qubit using a quantum circuit refrigerator, *Phys. Rev. Appl.* **20**, 044077 (2023).
- [31] T. Wang, F. Wu, F. Wang, X. Ma, G. Zhang, J. Chen, H. Deng, R. Gao, R. Hu, L. Ma, Z. Song, T. Xia, M. Ying, H. Zhan, H.-H. Zhao, and C. Deng, Efficient Initialization of Fluxonium Qubits based on Auxiliary Energy Levels, *Phys. Rev. Lett.* **132**, 230601 (2024).
- [32] V. Murya, H. Zhang, D. Kowsari, A. Kuo, D. M. Hartsell, C. Miyamoto, J. Liu, S. Shanto, E. Vlachos, A. Zarassi, K. W. Murch, and E. M. Levenson-Falk, On-Demand Driven Dissipation for Cavity Reset and Cooling, *PRX Quantum* **5**, 020321 (2024).
- [33] J. Ding, Y. Li, H. Wang, G. Xue, T. Su, C. Wang, W. Sun, F. Li, Y. Zhang, Y. Gao, J. Peng, Z. H. Jiang, Y. Yu, H. Yu, and F. Yan, Multipurpose architecture for fast reset and protective readout of superconducting qubits, *Phys. Rev. Appl.* **23**, 014012 (2025).
- [34] N. Lacroix, L. Hofele, A. Remm, O. Benhayoune-Khadraoui, A. McDonald, R. Shillito, S. Lazar, C. Hellings, F. m. c. Swiadek, D. Colao-Zanuz, A. Flasby, M. B. Panah, M. Kerschbaum, G. J. Norris, A. Blais, A. Wallraff, and S. Krinner, Fast Flux-Activated Leakage Reduction for Superconducting Quantum Circuits, *Phys. Rev. Lett.* **134**, 120601 (2025).
- [35] M. D. Reed, B. R. Johnson, A. A. Houck, L. DiCarlo, J. M. Chow, D. I. Schuster, L. Frunzio, and R. J. Schoelkopf, Fast reset and suppressing spontaneous emission of a superconducting qubit, *Appl. Phys. Lett.* **96**, 203110 (2010).
- [36] X. Yang, J. Chu, Z. Guo, W. Huang, Y. Liang, J. Liu, J. Qiu, X. Sun, Z. Tao, J. Zhang, J. Zhang, L. Zhang, Y. Zhou, W. Guo, L. Hu, J. Jiang, Y. Liu, X. Linpeng, T. Chen, Y. Chen, J. Niu, S. Liu, Y. Zhong, and D. Yu, Coupler-Assisted Leakage Reduction for Scalable Quantum Error Correction with Superconducting Qubits, *Phys. Rev. Lett.* **133**, 170601 (2024).
- [37] A. A. Clerk, M. H. Devoret, S. M. Girvin, F. Marquardt, and R. J. Schoelkopf, Introduction to quantum noise, measurement, and amplification, *Rev. Mod. Phys.* **82**, 1155 (2010).
- [38] D. Gao, D. Fan, C. Zha, J. Bei, G. Cai, J. Cai, S. Cao, F. Chen, J. Chen, K. Chen, X. Chen, X. Chen, Z. Chen, Z. Chen, Z. Chen, W. Chu, H. Deng, Z. Deng, P. Ding, X. Ding, Z. Ding, S. Dong, Y. Dong, B. Fan, Y. Fu, S. Gao, L. Ge, M. Gong, J. Gui, C. Guo, S. Guo, X. Guo, L. Han, T. He, L. Hong, Y. Hu, H.-L. Huang, Y.-H. Huo, T. Jiang, Z. Jiang, H. Jin, Y. Leng, D. Li, D. Li, F. Li, J. Li, J. Li, J. Li, J. Li, N. Li, S. Li, W. Li, Y. Li, Y. Li, F. Liang, X. Liang, N. Liao, J. Lin, W. Lin, D. Liu, H. Liu, M. Liu, X. Liu, X. Liu, Y. Liu, H. Lou, Y. Ma, L. Meng, H. Mou, K. Nan, B. Nie, M. Nie, J. Ning, L. Niu, W. Peng, H. Qian, H. Rong, T. Rong, H. Shen, Q. Shen, H. Su, F. Su, C. Sun, L. Sun, T. Sun, Y. Sun, Y. Tan, J. Tan, L. Tang, W. Tu, C. Wan, J. Wang, B. Wang, C. Wang, C. Wang, C. Wang, J. Wang, L. Wang, R. Wang, S. Wang, X. Wang, X. Wang, X. Wang, Y. Wang, Z. Wei, J. Wei, D. Wu, G. Wu, J. Wu, S. Wu, Y. Wu, S. Xie, L. Xin, Y. Xu, C. Xue, K. Yan, W. Yang, X. Yang, Y. Yang, Y. Ye, Z. Ye, C. Ying, J. Yu, Q. Yu, W. Yu, X. Zeng, S. Zhan, F. Zhang, H. Zhang, K. Zhang, P. Zhang, W. Zhang, Y. Zhang, Y. Zhang, L. Zhang, G. Zhao, P. Zhao, X. Zhao, X. Zhao, Y. Zhao, Z. Zhao, L. Zheng, F. Zhou, L. Zhou, N. Zhou, N. Zhou, S. Zhou, S. Zhou, Z. Zhou, C. Zhu, Q. Zhu, G. Zou, H. Zou, Q. Zhang, C.-Y. Lu, C.-Z. Peng, X. Zhu, and J.-W. Pan, Establishing a New Benchmark in Quantum Computational Advantage with 105-qubit Zuchongzhi 3.0 Processor, *Phys. Rev. Lett.* **134**, 090601 (2025).
- [39] R. Acharya, I. Aleiner, R. Allen, T. I. Andersen, M. Ansbmann, F. Arute, K. Arya, A. Asfaw, J. Atalaya, R. Babush, D. Bacon, J. C. Bardin, J. Basso, A. Bengtsson, S. Boixo, G. Bortoli, A. Bourassa, J. Bovaird, L. Brill, M. Broughton, B. B. Buckley, D. A. Buell, T. Burger, B. Burkett, N. Bushnell, Y. Chen, Z. Chen, B. Chiaro, J. Cogan, R. Collins, P. Conner, W. Courtney, A. L. Crook, B. Curtin, D. M. Debroy, A. D. T. Barba, S. Demura, A. Dunsworth, D. Eppens, C. Erickson, L. Faoro, E. Farhi, R. Fatemi, L. F. Burgos, E. Forati, A. G. Fowler, B. Foxen, W. Giang, C. Gidney, D. Gilboa, M. Giustina, A. G. Dau, J. A. Gross, S. Habegger, M. C. Hamilton, M. P. Harrigan, S. D. Harrington, O. Higgott, J. Hilton, M. Hoffmann, S. Hong, T. Huang, A. Huff, W. J. Huggins, L. B. Ioffe, S. V. Isakov, J. Iveland, E. Jeffrey, Z. Jiang, C. Jones, P. Juhas, D. Kafri, K. Kechedzhi, J. Kelly, T. Khattar, M. Khezri, M. Kieferova, S. Kim, A. Kitaev, P. V. Klimov, A. R. Klots, A. N. Korotkov, F. Kostritsa, J. M. Kreikebaum, D. Landhuis, P. Laptev, K.-M. Lau, L. Laws, J. Lee, K. Lee, B. J. Lester, A. Lill, W. Liu, A. Locharla, E. Lucero, F. D. Malone, J. Marshall, O. Martin, J. R. McClean, T. McCourt, M. McEwen, A. Megrant, B. M. Costa, X. Mi, K. C. Miao, M. Mohseni, S. Montazeri, A. Morvan, E. Mount, W. Mruczkiewicz, O. Naaman, M. Neeley, C. Neill, A. Nersisyan, H. Neven, M. Newman, J. H. Ng, A. Nguyen, M. Nguyen, M. Y. Niu, T. E.

- O'Brien, A. Opremcak, J. Platt, A. Petukhov, R. Potter, L. P. Pryadko, C. Quintana, P. Roushan, N. C. Rubin, N. Saei, D. Sank, K. Sankaragomathi, K. J. Satzinger, H. F. Schurkus, C. Schuster, M. J. Shearn, A. Shorter, V. Shvarts, J. Skrzuzny, V. Smelyanskiy, W. C. Smith, G. Sterling, D. Strain, M. Szalay, A. Torres, G. Vidal, B. Villalonga, C. V. Heidweiller, T. White, C. Xing, Z. J. Yao, P. Yeh, J. Yoo, G. Young, A. Zalcman, Y. Zhang, N. Zhu, and G. Q. AI, Suppressing quantum errors by scaling a surface code logical qubit, *Nature* **614**, 676 (2023).
- [40] D. Ristè, J. G. van Leeuwen, H.-S. Ku, K. W. Lehnert, and L. DiCarlo, Initialization by Measurement of a Superconducting Quantum Bit Circuit, *Phys. Rev. Lett.* **109**, 050507 (2012).
- [41] M. S. Moreira, G. G. Guerreschi, W. Vlothuizen, J. F. Marques, J. van Straten, S. P. Premaratne, X. Zou, H. Ali, N. Muthusubramanian, C. Zachariadis, J. van Someren, M. Beekman, N. Haider, A. Bruno, C. G. Almudever, A. Y. Matsuura, and L. DiCarlo, Realization of a quantum neural network using repeat-until-success circuits in a superconducting quantum processor, *npj Quantum Inf.* **9**, 118 (2023).
- [42] G. Kim, A. Butler, V. S. Ferreira, X. S. Zhang, A. Hadley, E. Kim, and O. Painter, Fast unconditional reset and leakage reduction of a tunable superconducting qubit via an engineered dissipative bath, *Phys. Rev. Appl.* , (2025).
- [43] M. McEwen, D. Kafri, Z. Chen, J. Atalaya, K. J. Satzinger, C. Quintana, P. Klimov, V. D. Sank, C. Gidney, A. G. Fowler, F. Arute, K. Arya, B. Buckley, B. Burkett, N. Bushnell, B. Chiaro, R. Collins, S. Demura, A. Dunsworth, C. Erickson, B. Foxen, M. Giustina, T. Huang, S. Hong, E. Jeffrey, S. Kim, K. Kechedzhi, F. Kostritsa, P. Laptev, A. Megrant, X. Mi, J. Mutus, O. Naaman, M. Neeley, C. Neill, M. Niu, A. Paler, N. Redd, P. Roushan, T. C. White, J. Yao, P. Yeh, A. Zalcman, Y. Chen, N. Smelyanskiy, J. M. Martinis, H. Neven, J. Kelly, A. N. Korotkov, A. G. Petukhov, and R. Barends, Removing leakage-induced correlated errors in superconducting quantum error correction, *Nat. Commun.* **12**, 1761 (2021).

Supplemental Material for “Flexible Readout and Unconditional Reset for Superconducting Multi-Qubit Processors with Tunable Purcell Filters”

Yong-Xi Xiao,^{1,2,*} Da'er Feng,^{1,2,*} Xu-Yang Gu,^{1,2} Gui-Han Liang,^{1,2} Ming-Chuan Wang,^{1,2} Zheng-Yu Peng,^{1,2} Bing-Jie Chen,^{1,2} Yu Yan,^{1,2} Zheng-Yang Mei,^{1,2} Si-Lu Zhao,^{1,2} Yi-Zhou Bu,^{1,2} Cheng-Lin Deng,^{1,2} Xiaohui Song,^{1,2} Dongning Zheng,^{1,2,3,4} Yu-Xiang Zhang,^{1,2} Yun-Hao Shi,¹ Zhongcheng Xiang,^{1,2,3,4,†} Kai Xu,^{1,2,3,4,5,‡} and Heng Fan^{1,2,3,4,5,§}

¹*Beijing National Laboratory for Condensed Matter Physics,*

Institute of Physics, Chinese Academy of Sciences, Beijing 100190, China

²*School of Physics, University of Chinese Academy of Sciences Beijing 100049, China*

³*Beijing Academy of Quantum Information Sciences, 100193 Beijing, China*

⁴*Hefei National Laboratory, 230088 Hefei, China*

⁵*Songshan Lake Materials Laboratory, 523808 Dongguan, Guangdong, China*

CONTENTS

I. Suppression of photon noise and Purcell effect	2
II. SQUID parameters calculation for tunable filter	3
III. Readout circuits parameter with purcell filter	4
IV. Other device parameters	6
V. Measurement and control setup	6
VI. Readout optimization procedure	8
VII. Reset experiment details	11
VIII. Analysis of reset error accumulation	17
References	18

* These authors contributed equally to this work.

† zcxiang@iphy.ac.cn

‡ kaixu@iphy.ac.cn

§ hfan@iphy.ac.cn

I. SUPPRESSION OF PHOTON NOISE AND PURCELL EFFECT

The photon-noise-induced dephasing rate is governed by [1]:

$$\Gamma_{\phi}^{\text{noise}} = \frac{\kappa_{\text{eff}}(2\chi)^2}{\kappa_{\text{eff}}^2 + (2\chi)^2} \bar{n}_{\text{noise}}, \quad (\text{S1})$$

where \bar{n}_{noise} is the average photon noise number. When $\kappa_{\text{eff}} = 2\chi$, the dephasing rate reaches its maximum (Γ_{max}). Tunable filters maintain $\kappa \neq 2\chi$ during non-readout periods, ensuring $\Gamma_{\text{tunable}} < \Gamma_{\text{max}}$, whereas fixed-frequency filters persistently operate at $\kappa = 2\chi$ when qubit frequency is fixed, yielding $\Gamma_{\text{linear}} = \Gamma_{\text{max}}$. Thus, tunable nonlinear filters more effectively suppress photon noise propagation from transmission lines into readout resonators, thereby suppress qubit dephasing. To verify the frequency-tunable filter's suppression effect on photon noise, we intentionally inject Gaussian white noise into the readout transmission line. The noise spectrum is confined within ± 500 MHz of the readout frequency, with amplitudes following a discrete Gaussian distribution (mean = 0, standard deviation = 0.05) sampled at 0.5 ns intervals. We then measure and fit the qubit's dephasing rate.

Notably, the qubit in this experiment is frequency-tunable. We set the operating frequency of this qubit at a position below the vertex, which requires continuous flux bias to maintain. To better characterize how the dephasing time varies with Gaussian noise intensity, we employed a Carr-Purcell-Meiboom-Gill (CPMG) sequence ($n=3$) to mitigate flux bias interference, so called 1/f-type noise.

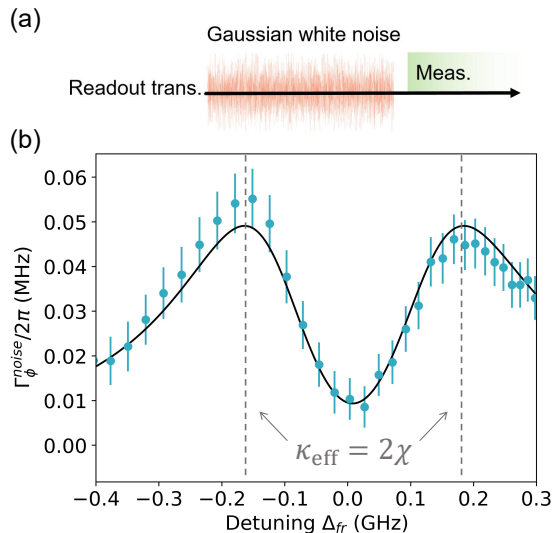


FIG. S1. Evaluation of the noise tolerance. (a) Readout pulse sequence. The qubit T_2 is measured while applying Gaussian white noise through the readout transmission line. (b) Qubit dephasing rate versus detuning. The black curve represents a fit with Eq. (S1), where \bar{n}_{noise} is regressed as a constant.

Measurement data under different detunings of filter and readout resonator are shown in Fig. S1, with error bars representing uncertainties in dephasing rate fitting. Error sources include residual flux bias and artificial noise amplitude fluctuations. The two peaks correspond to readout points at $\kappa_{\text{eff}} = 2\chi$. Smaller detunings exhibit reduced dephasing rates due to excessive κ_{eff} , while larger detunings show decreased rates from insufficient κ_{eff} . Black curves in the figure represent fits using Eq. (S1) assuming \bar{n}_{noise} as a constant. The agreement between experimental data and theoretical predictions confirms the validity of photon noise suppression through frequency-tunable filters. Observed different peak height is attributed to photon absorption by other resonators sharing the same filter and increased transmission impedance at higher frequencies.

Tunable filter applications for multi-qubit dephasing suppression manifest in three aspects: First, in surface code implementations using measurement ancilla qubits for error correction, the filter protects data qubits from measurement-induced dephasing. Second, a protection window is created during post-measurement photon dissipation where nonlinear filter frequency shift caused by decreasing photon numbers automatically reduces dephasing rate. Third, dephasing caused by non-ideal photon noise inputs is suppressed.

In the absence of a Purcell filter, the photon decay rate is expressed as:

$$\Gamma = \kappa_r \left(\frac{g_{qr}}{\Delta_{qr}} \right)^2. \quad (\text{S2})$$

For samples incorporating a Purcell filter, the qubit photon decay rate induced by the Purcell effect is given by: [2]

$$\Gamma_{01,\text{Purcell}} = \kappa_{\text{eff}} \frac{g_{qr}^2}{(\omega_r - \omega_q)^2} \quad (\text{S3})$$

$$= \frac{4|g_{fr}|^2 \kappa_f}{\kappa_f^2 + 4(\omega_f - \omega_q)^2} \frac{g_{qr}^2}{(\omega_r - \omega_q)^2}. \quad (\text{S4})$$

The suppression of photon decay by fixed-frequency linear filters has been extensively discussed in prior studies. Here, we focus on comparing the difference between tunable nonlinear filter and fixed linear filter. For a fixed-frequency linear filter, the design typically requires $\omega_f \approx \omega_r$ with $\kappa = 2\chi$. In contrast, a frequency-tunable nonlinear filter are not subject to such stringent constraints during non-readout periods, allowing a larger detuning from the qubit frequency. For instance, consider a scenario where both fixed-frequency filter and readout resonator operate at 6.5 GHz, while the tunable filter remains at 7 GHz (at idle point), with the qubit frequency at 5.5 GHz. The linewidth of both filters is the same $\kappa_f/2\pi = 150$ MHz. The eq. (S3)-derived result is:

$$\frac{\Gamma_{\text{fixed,Purcell}}}{\Gamma_{\text{tunable,Purcell}}} \approx 2.08, \quad (\text{S5})$$

which demonstrates that the larger detuning enabled by a tunable filter provides enhanced suppression of the Purcell effect compared to a fixed-frequency filter.

II. SQUID PARAMETERS CALCULATION FOR TUNABLE FILTER

The filter is a $\lambda/2$ open-circuit cavity. A SQUID is embedded at the midpoint, enabling tunable cavity frequency by varying the magnetic flux. First, consider the case without the SQUID: Let l denote the total cavity length, i.e., $l = \lambda/2$. The per-unit-length inductance and capacitance of the cavity are L_u and C_u , respectively, with a resonant frequency of $\omega_0 = \pi/(l\sqrt{L_u C_u})$. For a position z along the cavity (measured from the open end), the voltage and current are given by [3]:

$$V(z) = V_o \cos(\beta_0 z), \quad (\text{S6})$$

$$I(z) = -\frac{jV_o}{Z_0} \sin(\beta_0 z), \quad (\text{S7})$$

where V_0 is the voltage amplitude, $Z_0 = \sqrt{L_u/C_u}$ is the characteristic impedance of the transmission line, $\beta_0 = \omega_0/v_p$ is the wave vector, and v_p is the phase velocity. At the midpoint $z = l/2$, the voltage is zero. When a SQUID is inserted at the cavity midpoint $z = l/2$, the resonant frequency shifts to ω . The SQUID is approximated as a point element that does not alter the cavity length. It introduces a voltage discontinuity at $z = l/2$, with voltages on either side given by:

$$V_{l/2}^{\pm} = \pm V_o \cos\left(\frac{\beta l}{2}\right), \quad (\text{S8})$$

where $\beta = \omega/v_p$ is the new resonant wave vector. The SQUID behaves as a superconducting inductance L_S with impedance:

$$Z_S = j\omega L_S. \quad (\text{S9})$$

This impedance equals the ratio of the voltage difference across the SQUID to the current through it:

$$\frac{2V_o \cos\left(\frac{\beta l}{2}\right)}{-\frac{jV_o}{Z_0} \sin\left(\frac{\beta l}{2}\right)} = j\omega L_S, \quad (\text{S10})$$

substituting $2\pi Z_0 = 2l\omega_0 L_u$ yields:

$$\cot\left(\frac{\pi \omega}{2 \omega_0}\right) = \frac{\pi L_s \omega}{2 L_u l \omega_0}. \quad (\text{S11})$$

Under the condition $(\omega_0 - \omega) \ll \omega_0$, we have

$$\cot\left(\frac{\beta l}{2}\right) \ll 1, \quad (\text{S12})$$

allowing the approximation:

$$\omega = \frac{\omega_0}{1 + \frac{L_s}{L_u l}}. \quad (\text{S13})$$

where $\omega_0 = \pi/(\sqrt{L_u C_u} l)$, L_u and C_u represent the per-unit-length inductance and capacitance of the coplanar waveguide. This demonstrates the dependence of the filter's passband frequency on the applied magnetic flux bias. L_s denotes the SQUID-induced inductance: [4, 5]

$$L_s = \frac{\Phi_0}{2\pi \sqrt{(I_{c1} - I_{c2})^2 + 4I_{c1}I_{c2} \cos^2(\pi\Phi/\Phi_0)}}, \quad (\text{S14})$$

where I_{c1} and I_{c2} are the critical currents of the asymmetric junctions, Φ is the flux and $\Phi_0 = h/(2e)$. Notably, the filter frequency is primarily controlled by magnetic flux. Given the minimal anharmonicity of the filter, the frequency shift induced by readout pulse power variation remains relatively small, requiring only minor compensation through magnetic flux bias for correction.

III. READOUT CIRCUITS PARAMETER WITH PURCELL FILTER

The circuit design considers the respective parameters of the qubit, readout resonator, and filter, as well as their interaction. A general approach is as follows:

First, a target effective readout resonator linewidth κ_{eff} is specified based on readout time requirements, which simultaneously defines the matching readout resonator dispersive shift $2\chi = \kappa_{\text{eff}}$. The dispersive shift typically falls within the MHz range in multi-qubit devices to balance the readout SNR and the qubit protection. This target value is then converted to fundamental circuit parameters. Using the formula [6]:

$$\kappa_{\text{eff}} = \frac{4|g_{rf}|^2}{\kappa_f} \frac{1}{1 + (2\Delta_{fd}/\kappa_f)^2}, \quad (\text{S15})$$

an equation is established relating the coupling strength g_{rf} between readout resonator and filter, the frequency detuning $\Delta_{fd} = \omega_f - \omega_r$ between filter and resonator, and the filter's linewidth κ_f . For systems dominated by capacitive coupling, the coupling strength between the readout resonator and the filter is given by:

$$g_{rf} = \frac{1}{2} C_{rf} \sqrt{\frac{\omega_r \omega_f}{C_r C_f}}, \quad (\text{S16})$$

where C_{rf} represents the mutual capacitance between filter and readout resonator, while C_f and C_r denote the equivalent ground capacitances at the coupling points of the filter and readout resonator, respectively.

The filter linewidth is determined by:

$$\kappa_f = \frac{\omega_f}{Q_f}, \quad Q_f = \frac{C_f^{\text{out}}}{\omega_f Z_0 C_{\text{out}}}. \quad (\text{S17})$$

Here, C_{out} represents the coupling capacitance between filter output port and transmission line, and C_f^{out} is the equivalent ground capacitance at the filter's output port. The condition $C_{\text{out}} \gg C_{\text{in}}$ is typically satisfied in S21 readout schemes to ensure most of the readout signal propagates towards the output port, which is essential for performing transmission readout with high measurement efficiency [5, 7]. Notably, for a $\lambda/2$ filter cavity in GHz frequency range (with mm-scale physical length), the

spatial distribution of electric field must be carefully considered when determining equivalent ground capacitance at different positions. This can be efficiently analyzed using transmission line Y-parameters: when injecting a microwave signal at a specific position, the admittance parameter at that point satisfies [3]:

$$Y_{11} = j2C(\omega - \omega_0), \quad (\text{S18})$$

where the slope of the imaginary part of Y_{11} versus frequency ω directly yields twice the equivalent ground capacitance. This method enables accurate determination of capacitance values through simulation or experimental characterization.

Furthermore, the dispersive shifts are different for O1 and O2 measurements [8, 9]. In dispersive regime, the dressed modes of a readout resonator are:

$$\omega_{r,0} = \omega_r - \chi_{0,1}, \quad (\text{S19})$$

$$\omega_{r,1} = \omega_r + \chi_{0,1} - \chi_{1,2}, \quad (\text{S20})$$

$$\omega_{r,2} = \omega_r + \chi_{1,2} - \chi_{2,3}, \quad (\text{S21})$$

where ω_r is bare mode and $\chi_{i,j}$ is given by:

$$\chi_{ij} = \frac{g_{ij}^2}{\omega_{ij} - \omega_r}. \quad (\text{S22})$$

Using the relation:

$$g_{j,j+1} \propto \sqrt{\frac{j+1}{2}} \left(\frac{E_j}{8EC} \right)^{1/4}, \quad (\text{S23})$$

the shift we need can be expressed by:

$$\chi_{0,1} = \frac{g^2}{\omega_{0 \rightarrow 1} - \omega_r}, \quad (\text{S24})$$

$$\chi_{1,2} = \frac{2g^2}{\omega_{1 \rightarrow 2} - \omega_r}, \quad (\text{S25})$$

$$\chi_{2,3} = \frac{3g^2}{\omega_{2 \rightarrow 3} - \omega_r}, \quad (\text{S26})$$

where the qubit-readout resonator coupling strength is:

$$g = \frac{1}{2} C_{qr} \sqrt{\frac{\omega_q \omega_r}{C_q C_r}}. \quad (\text{S27})$$

Thus, the dispersive shifts for O1 and O2 measurement can be calculated by:

$$2\chi = \omega_{r,1} - \omega_{r,0}, \quad (\text{S28})$$

$$2\chi' = \omega_{r,2} - \omega_{r,0}. \quad (\text{S29})$$

We have now formulated κ_{eff} and 2χ (for O1 and O2 measurement) in the context of circuit parameters.

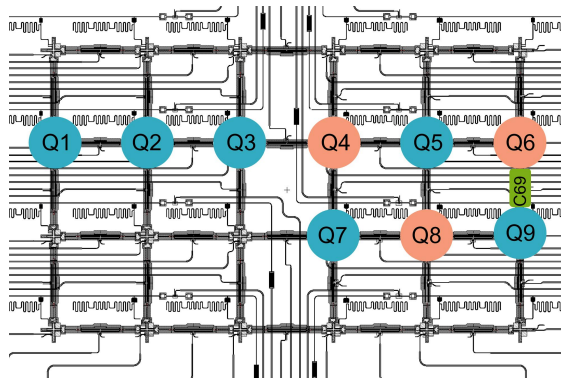


FIG. S2. Flip-chip sample diagram, where air bridges and indium bumps are intentionally omitted for clarity. The nine experimentally calibrated qubits with tunable frequencies are color-coded. Blue indicates qubits with a designed vertex frequency of 5.1 GHz, while orange represents those with a designed vertex frequency of 4.5 GHz. The reset scheme is implemented by C69 (marked in green)

IV. OTHER DEVICE PARAMETERS

The experimental device is fabricated with a total of 24 qubits, employing the scalable coupling scheme proposed in Ref. [10]. Due to limited measurement and control equipment time, we selected 9 qubits as shown in Fig. S2, along with some connected couplers, for preliminary calibration.

To investigate how different coupling capacitances between couplers and filters affect reset performance, we design various capacitive coupling strengths, with effective mutual capacitance values ranging from 0.64 fF to 2.4 fF. Considering different coupling positions on the filters, the coupling strength varies approximately from 4 MHz to 20 MHz. C69 represents the design with maximum coupling strength, enabling the fastest coupler reset. We focused on optimizing measurement and control parameters for C69 and its two adjacent qubits Q6 and Q9. Q6 has a higher frequency, making it suitable as an ancillary qubit in surface code for readout and reset during parity check cycles. Therefore, the readout data presented in the main text comes from Q6, while reset results are from Q6 and C69. And the evaluation of the noise tolerance is from Q9.

No significant impact of $g_{cf}/2\pi \leq 20$ MHz on normal qubit and coupler operations is observed experimentally. This is because during non-reset operations, the filter maintains large detuning from both qubits and couplers. Main parameters are shown in Tab. S1. Note that, the value of 2χ obtained from the chi-kappa-power experiment [11] is slightly different from that obtained by scanning S21 of dressed modes. Here we show the result from S21. The readout fidelities of qubits other than Q6 and Q9 have not been fully optimized and could be further improved. The design parameters of all filters on the device are nearly identical, as listed in Tab. S2. Taking Q6's readout resonator as an example, the κ_{eff} implemented by the filter is tunable between 0.2-11.5 MHz with a coupling of $g_{rf}/2\pi \approx 20$ MHz. I_c represents the Josephson junction critical current, which quantifies the nonlinearity introduced to the filter by the SQUID. Following ref. [12], the distributed-element circuit of the filter can be equivalently modeled as a lumped LCR circuit, thereby enabling the calculation of anharmonicity.

TABLE S1. Device parameters for Q_6 - C_{69} - Q_9 and means of Q_1 - Q_9 on flip-chip superconducting processor.

	Q_6	C_{69}	Q_9	Q_{1-9}^{mean}
$\omega_{1,0}^{\text{idle}}/2\pi$ (GHz)	4.835	8.597	4.021	4.551
$\alpha/2\pi$ (MHz)	188	120	193	190
T_1^{idle} (μs)	35.6	7.3	48.3	45.1
T_2^{CPMG} (μs)	19.03		46.62	38.11
$\omega_r/2\pi$ (GHz)	6.454		6.545	6.595
$2\chi_{1,0}/2\pi$ (MHz)	1.4		1.1	1.2
$F_{\text{meas.}}$ (%)	99.3		98.1	96.7

V. MEASUREMENT AND CONTROL SETUP

The quantum device is integrated into a BlueFors dilution refrigerator (DR) system, with the mixing chamber plate (MC) stabilized at a base temperature of approximately 7~13 mK. Standard cryogenic wiring configurations are implemented for all qubit and tunable coupler control lines as well as tunable filter flux control lines to ensure optimal device performance. The

TABLE S2. Parameters for Purcell filter.

	Quantity		Units
C_{in}	Input capacitance	15.7	fF
C_{out}	Output capacitance	106.5	fF
I_c	Critical current of SQUID	0.4	μA
I_{c1}	Critical current of Jose. junc. 1	0.085	μA
I_{c2}	Critical current of Jose. junc. 2	0.315	μA
$\omega_0/2\pi$	Frequency without SQUID	9.3	GHz
$\omega_{biasZ}/2\pi$	Frequency range tuned by biasZ	6.02-7.06	GHz
$\alpha_f/2\pi$	Anharmonicity of filter	4.47	MHz
$\kappa_f/2\pi$	Linewidth of filter	150	MHz
L_u	Per-unit-length inductance	464	nH
C_u	Per-unit-length capacitance	203	pF

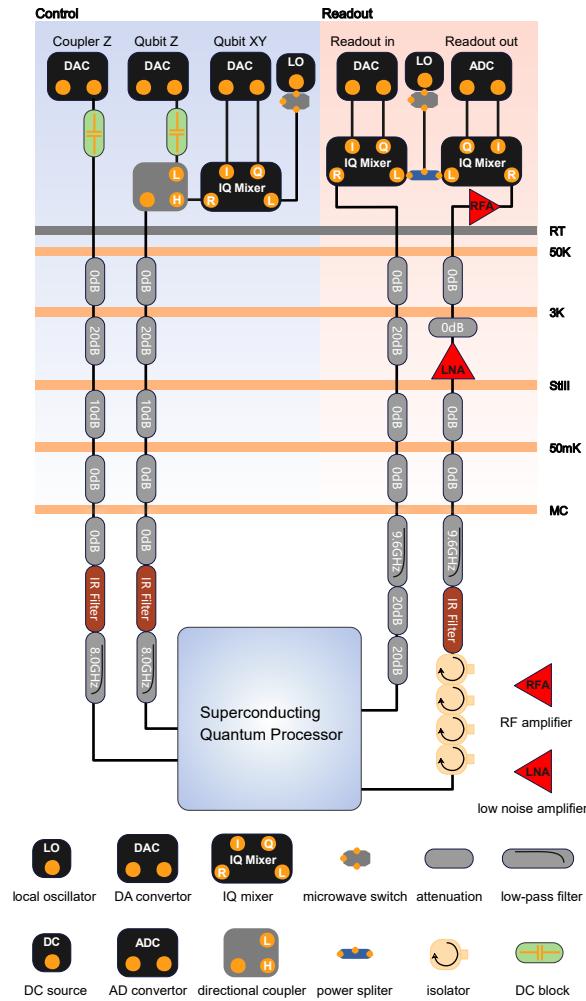


FIG. S3. Cryogenic and room temperature wiring

configuration of the tunable filter flux control lines is the same as that of the couplers. Comprehensive microwave attenuation and filtering networks are installed to suppress Johnson-Nyquist noise and higher-order harmonic interference. A multiplexed readout architecture is employed, featuring a common feedline shared among qubits, with four-stage isolation and a cryogenic low-noise amplifier (LNA) for signal enhancement. Notably, there is no quantum-limited amplifier like JPAs or TWPAs.

The experimental sequence is orchestrated by a centralized control system. All microwave control pulses are synthesized using a combination of digital-to-analog converters (DACs) and upconversion through local oscillator (LO) mixing. The resulting quantum signals are subsequently demodulated by LO signal and digitized by analog-to-digital converters (ADCs) for data

acquisition and analysis. A schematic representation of the complete experimental setup is provided in Fig. S3.

VI. READOUT OPTIMIZATION PROCEDURE

The tunable Purcell filter introduces an extra degree of freedom for tuning κ_{eff} to achieve $2\chi \approx \kappa_{\text{eff}}$, and it also provides enhancement on readout fidelity via bifurcation due to its nonlinearity. The readout optimization procedure is much more complex since the flux bias voltage of tunable Purcell filter, the resonator drive (readout) frequency and the resonator drive (readout) power are highly correlated. For conventional fixed-frequency linear Purcell filter, performing parameter scans with respect to resonator drive frequency and power would usually make for the majority of improvement on readout fidelity. However, with tunable Purcell filter, the frequency of which is highly detuned from the resonators when no flux bias is applied, we need to jointly optimize flux bias with these parameters, and the frequency of the Purcell filter would significantly affect readout SNR. As performing parameter scan for more than two dimensions is time consuming, we can opt to alternately sweep different two of the parameter dimensions and iteratively converge toward a near-optimal parameter set.

For illustration, we fix one of the parameters and scan a broad range of the other two parameters. The relationship between these parameters and readout fidelity is shown in Fig. S4. As the power increases, bistability of the resonator field emerges, mainly due to high-order nonlinear terms of the qubit-resonator interaction, consistent with the phenomenon reported in ref. [13]. Consequently, at the same readout power level, two distinct frequency regions are available for achieving relatively high readout fidelity, as is shown in Fig. S4(a). The lower-frequency region exhibits superior readout fidelity, primarily attributed to its deeper dip characteristic. The two regions of Z pulse amplitude to reach high readout fidelity at high readout power in Fig. S4(b) can also be explained by the bistability of the resonator field, where the conditions $2\chi = \kappa_{\text{eff}}$ for the two dips are reached for two different filter Z pulse amplitudes respectively. The two resonator dips shift to diverse directions when readout power is increased, and thus it requires to compensate this frequency shift by tuning the filter's frequency. For low readout power, however, the bistability vanishes, thus there is only one region for optimal readout fidelity under certain readout power. As the frequency of the tunable Purcell filter get close to the resonator frequency, anticross pattern of the resonator-filter system occurs, and there are two frequency branches that can reach high readout fidelity, as depicted in Fig. S4(c).

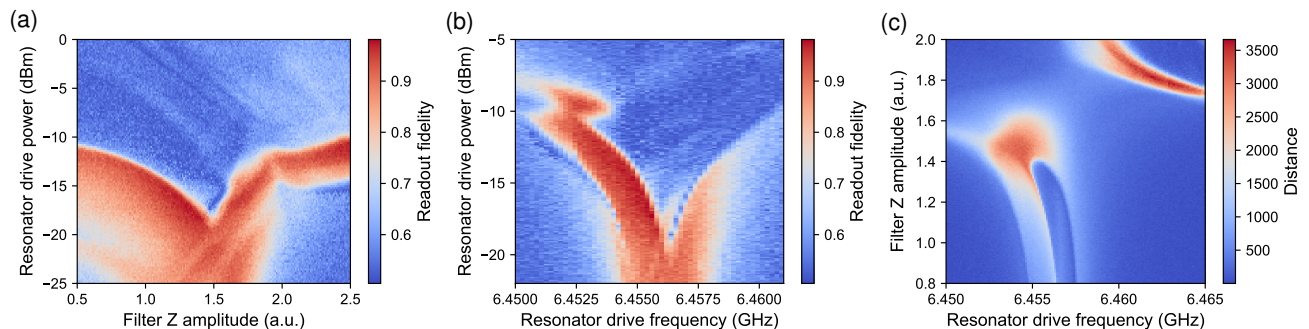


FIG. S4. The relation of resonator drive frequency, power and filter flux bias (Z) amplitude to readout fidelity or distance between readout signal centers of $|0\rangle$ and $|1\rangle$. (a) Readout fidelity under different resonator drive power and frequency with filter Z amplitude being 1.32. (b) Readout fidelity under different resonator drive power and filter Z amplitude with resonator drive frequency being 6.4554 GHz. (c) Distance between average values of readout signal of state $|0\rangle$ and $|1\rangle$ with resonator drive power -17.4 dBm.

The readout time also play a crucial role in readout fidelity, as we need to strike a balance between high SNR and low qubit state transition rate during the readout process, and lowering readout time consumption allows more operations under the limited decoherence time, especially in scenarios where readout is applied multiple times such as quantum error corrections. Parameter scan result for readout time and power is presented in Fig. S5. When the readout time is reduced, high readout fidelity can still be reached by slightly increasing readout power. Additionally, applying ring-up pulse and dynamically tuning qubit flux control can improve SNR and reduce state transition rate, respectively. In such scenario requiring simultaneous optimization of multiple variables, employing grid search (parameter scan) inevitably explores extensive low-fidelity parameter subspaces. Beyond conventional coarse-to-fine scanning with alternating iterative parameter optimization for each parameters, Bayesian optimization offers automated parameter exploration. We utilize the Tree-structured Parzen Estimator algorithm from the Optuna package [14], which can operate within predefined parameter ranges to autonomously identify relatively optimal hyperparameter configurations. Compared to manual iterative optimization, heuristic approaches, and traditional gradient-free algorithms, its advantage lies in the capacity to explore multiple high-potential regions while avoiding persistent entrapment in local minima. This methodology discovers multiple distinct relatively optimal parameter combinations, which is explainable

TABLE S3. Selected optimal readout parameters for 500ns and 1077ns readout.

Readout time (ns)	500	1077
Filter readout ZPA	0.680367	1.576001
Qubit readout ZPA	0.440191	0.035742
Readout pulse power (dBm)	-1.0349	-16.9254
Ring-up pulse power (dBm)	6.5958	-22.5849
Ring-up pulse time length (ns)	12.0	65.0
Readout frequency (GHz)	6.452666	6.453746

TABLE S4. Error budget analysis of qubit readout with optimal parameters for 500ns $|0\rangle$ -versus- $|1\rangle$ and $|0\rangle$ -versus- $|2\rangle$ readout and 1077ns $|0\rangle$ -versus- $|2\rangle$ readout with post selection.

	500 ns (01)	500 ns (02)	1077 ns (02)
readout fidelity	97.37%	98.03%	99.3%
state $ 0\rangle$ fidelity	98.95%	99.36%	99.65%
state $ 1\rangle$ fidelity	95.78%	96.70%	98.96%
separation error	0.147%	0.038%	0.0132%
state error	2.485%	1.929%	0.682%
energy relaxation	1.782%	$\leq 1.782\%$	$\leq 3.798\%$

since we observe several regions with comparatively high fidelity in the preceding parameter scan.

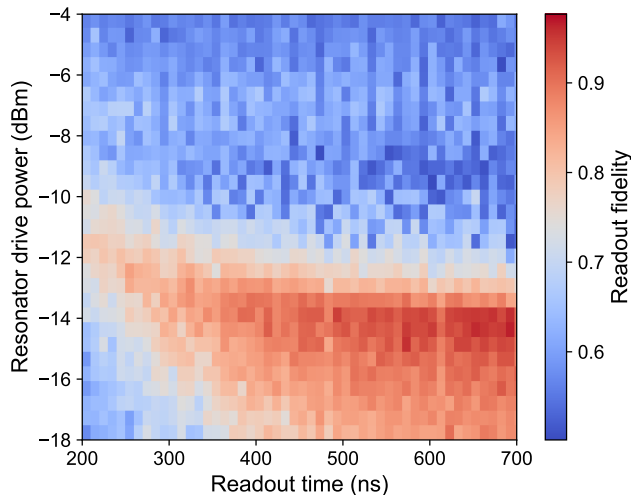


FIG. S5. Parameter scan of readout fidelity with respect to readout time and resonator drive power.

We select readout pulse length of 500 ns and allow the readout time to vary within a 2000 ns, respectively, and search for optimal readout parameters via Bayesian optimization. For the latter, we identify 1077 ns as the pulse duration yielding superior readout fidelity through optimization. We find optimal filter readout ZPA from two different regions, indicating both of the branches can reach high readout fidelity. The selected parameters and the corresponding error budgets are listed in Table S3 and S4. The ring-up pulse consists of a Gaussian envelope with 75 ns full-width at half-maximum (FWHM), symmetrically truncated with respect to its central axis within the ring pulse time length interval, which is superimposed at the beginning of the smoothed square readout pulse with a duration of the total readout length and 10ns FWHM Gaussian smoothing. The readout power refers to the output power level from the DACs. The abbreviation readout ZPA denotes the amplitude of the Z pulse applied during readout, maintaining temporal alignment with the readout pulse duration. The separation error quantifies the misclassification arising from the overlap region of the approximately Gaussian distributions characterizing the readout IQ data for the prepared $|0\rangle$ and $|1\rangle$ (or $|2\rangle$) states. Conversely, the state error represents the residual misclassification rate, primarily originating from state transitions during readout and state preparation errors such as imperfect π pulse and residual excitation. A portion of the transition error stems from energy relaxation, which can be estimated by $\epsilon_{T_1} = 1 - \exp(-\tau_m/T_1)$ with the readout time τ_m and the calibrated $T_1 \approx 27.812 \mu\text{s}$ of state $|1\rangle$ relaxation at current qubit frequency. For $|0\rangle$ -versus- $|2\rangle$ readout, however, the relaxation-induced error rate from the $|2\rangle$ state to the $|1\rangle$ state remains uncalibrated. While the state is initially

prepared in state $|2\rangle$, it takes two stages of relaxation to transition to state $|0\rangle$, i.e., $|2\rangle \rightarrow |1\rangle$ and $|1\rangle \rightarrow |0\rangle$; consequently, energy relaxation errors are upper bounded by the state $|1\rangle$ relaxation error. Furthermore, the misclassification rate depends critically on the placement of the discrimination threshold. Rather than selecting the perpendicular bisector between the $|0\rangle$ and $|1\rangle$ state IQ centroids, we optimize readout fidelity by deliberately offsetting the threshold toward state $|0\rangle$. This compensates for fidelity loss caused by relaxations which pulls and distorts the distribution of $|1\rangle$ state data points towards $|0\rangle$'s centroid. While this threshold optimization enhances average readout fidelity, it unavoidably lowers the $|0\rangle$ -state fidelity. This explains why the $|0\rangle$ -state fidelity may remain suboptimal despite its low state transition rate and minimal separation error contribution.

Furthermore, we demonstrate multiplexed joint dispersive readout of multi-qubits by simultaneously applying multi-frequency readout pulses and then demodulating the acquired signals to extract measured qubit states respectively. Limited by Purcell filter linewidth κ_f , this experiment only achieved optimized results for two-qubit joint readout, as shown in Fig. S6. The result indicates that tunable Purcell filter supports high-fidelity joint readout. Future extensions to high-fidelity joint readout of more qubits would require either increasing κ_f or incorporating broadband filter designs [15].

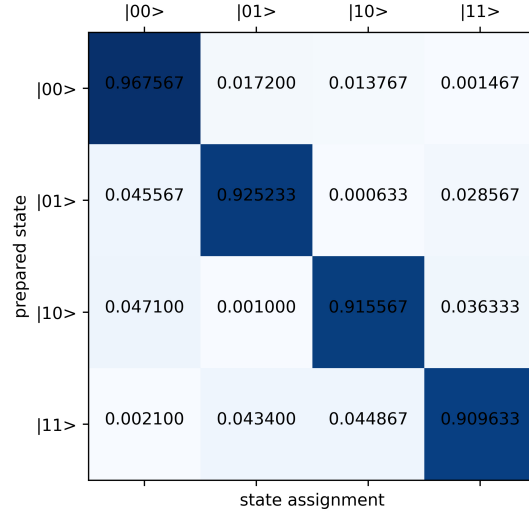


FIG. S6. Joint readout fidelity of Q4 and Q6 from 30000 times single shot.

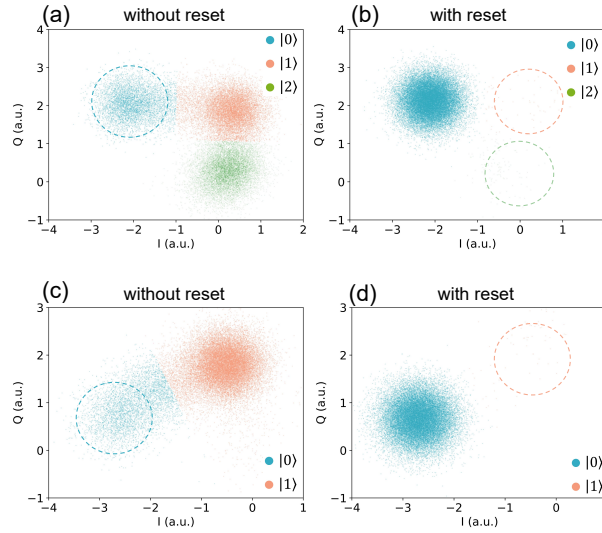


FIG. S7. Raw IQ data with (without) 1 cycle of reset. (a,b) Initial state with prepared both $|2\rangle$ and $|1\rangle$ excitation. (c,d) Initial state with only $|1\rangle$ excitation.

VII. RESET EXPERIMENT DETAILS

The procedure of finding parameters for qubit reset is similar to ref. [16]. We adopt flat square pulse and adiabatic pulse to perform qubit-coupler swap, and perform coupler-filter swap right after qubit-coupler swap with flat and ramp pulse, for unconditionally resetting state $|1\rangle$ and both $|1\rangle$ and $|2\rangle$, respectively.

The flat pulses enable direct on-resonance exchange of a single excitation from qubit to coupler and then from coupler to the Purcell filter, which is simple to implement and fast for resetting only state $|1\rangle$. While for unconditionally resetting both the $|1\rangle$ and $|2\rangle$ excitations of the qubit, the resonance exchange method is inadequate for achieving complete transfer of both the $|1\rangle$ and $|2\rangle$ excitations from qubit to coupler in one qubit-coupler swap stage, whereas the adiabatic exchange method is more preferable. Before the reset operation, the qubit state is in arbitrary superposition of $|1\rangle$ and $|2\rangle$. And then we adiabatically tune the coupler frequency from below to above the qubit frequency, during which the dressed eigenstates of the interacting qubit-coupler system exhibit negligible probability transfer. In the eigenbasis of the non-interacting qubit and coupler Hamiltonian, two of the dressed eigenstates predominately overlap with $|1_q 0_c\rangle$ and $|2_q 0_c\rangle$ before the exchange, and predominately overlap with $|0_q 1_c\rangle$ and $|0_q 2_c\rangle$ after the exchange, respectively, thereby accomplishing the simultaneous population transfer of both $|1\rangle$ and $|2\rangle$ states from the qubit to the coupler. The same adiabatic protocol can be applied to the coupler-filter swap stage as well.

The adiabatic qubit-coupler swap pulse shape we use is derived in [16], which is similar to the Roland and Cerf protocol. For a qubit-coupler system with Hamiltonian

$$H_{qc}^{(1)}(t) = \hbar \begin{bmatrix} \Delta(t)/2 & g_{qc} \\ g_{qc} & -\Delta(t)/2 \end{bmatrix} \quad (\text{S30})$$

in $\{|0_q 1_c\rangle, |1_q 0_c\rangle\}$ subspace, where g_{qc} is the qubit-coupler coupling strength, and $\Delta(t) = \omega_c(t) - \omega_q$ is their $|0\rangle$ - $|1\rangle$ transition frequency detuning. To satisfy adiabatic condition, a small scaling prefactor $\beta \ll 1$ is introduced, such that

$$|\partial_t \Delta(t)| = \beta (\Delta^2(t) + 4g_{qc}^2)^{\frac{3}{2}} / g_{qc}. \quad (\text{S31})$$

While considering the reset of state $|2\rangle$, the qubit-coupler Hamiltonian in the subspace with conservative excitation number 2, whose bases are $\{|0_q 2_c\rangle, |1_q 1_c\rangle, |2_q 0_c\rangle\}$, is given by

$$H_{qc}^{(2)} = \hbar \begin{bmatrix} \Delta(t) - E_C^c/\hbar & \sqrt{2}g_{qc} & 0 \\ \sqrt{2}g_{qc} & 0 & \sqrt{2}g_{qc} \\ 0 & \sqrt{2}g_{qc} & -\Delta(t) - E_C^q/\hbar \end{bmatrix}, \quad (\text{S32})$$

where E_C^q and E_C^c are the charging energies of the qubit and the coupler. Anticrosses of the energy levels of the dressed eigenstates take place round $\Delta(t) = E_C^c/\hbar$ and $\Delta(t) = -E_C^q/\hbar$. Similar condition $|\partial_t \Delta(t)| = \beta' ((\Delta(t) - \Omega_C)^2 + 8g_{qc}^2)^{\frac{3}{2}} / (\sqrt{2}g_{qc})$, $\beta' \ll 1$ should preserve near the anticrosses to ensure adiabaticity, where Ω_C can be E_C^c/\hbar or $-E_C^q/\hbar$. In our experimental setting, $E_C^q/(2\pi\hbar) = 187.394$ MHz and $E_C^c/(2\pi\hbar) = 330$ MHz. The approximation of the energy gap at the neighbourhood is valid if the two anticross frequencies are far apart enough. For simplicity, the frequency trajectory of the coupler can be derived by only considering the anticross of the dressed states $|0_q 1_c\rangle$ and $|1_q 0_c\rangle$ at $\Delta(t) = 0$, and the adiabaticity can be well preserved as long as the trajectory varies adequately slow around $\Delta(t) = E_C^c/\hbar$ and $\Delta(t) = -E_C^q/\hbar$. Numerical diagonalization of the qubit-coupler Hamiltonian yields the energy spectrum in Fig. S8.

If $\Delta(t)$ satisfies the boundary condition $\Delta(0) = \omega_0 = 2\pi f_0$ and $\Delta(\tau) = \omega_\tau = 2\pi f_\tau$, the solution of Eq. S31 is

$$\Delta(t) = -\frac{8g(\beta g t + \delta)}{\sqrt{1 - 16(\beta g t)^2 - 32\beta\delta g t - 16\delta^2}}, \quad (\text{S33})$$

with

$$\beta = \frac{-4\delta(\omega_\tau^2 + 4g^2) - \omega_\tau \sqrt{\omega_\tau^2 + 4g^2}}{4g\tau(\omega_\tau^2 + 4g^2)}, \quad (\text{S34})$$

$$\delta = -\frac{\omega_0}{\sqrt{16\omega_0^2 + 64g^2}}, \quad (\text{S35})$$

and $g := g_{qc}$. For state $|2\rangle$ reset, the solutions can be obtained by taking the substitutions $g \mapsto \sqrt{2}g_{qc}$ and $\Delta(t) \mapsto \Delta(t) - \Omega_C$. The Z pulse amplitude $Z_c(t)$ for the coupler flux control line needed is related to the coupler frequency $\omega_c(t)$ by

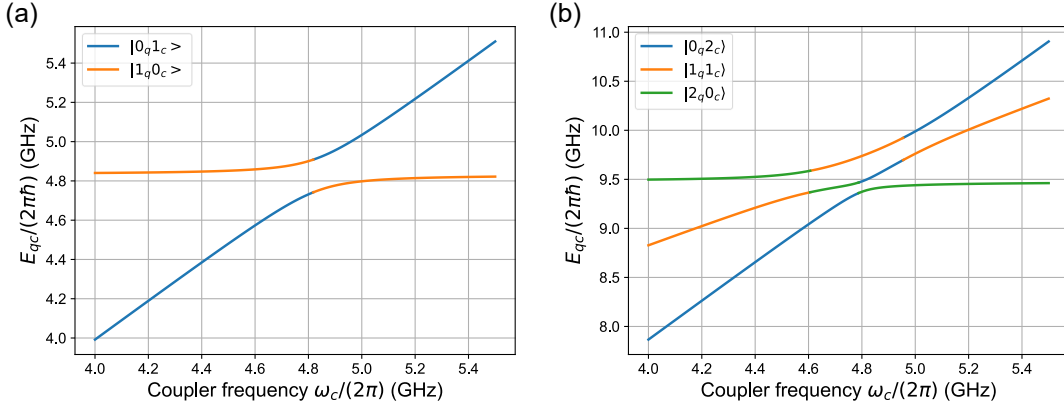


FIG. S8. Energy spectrum of qubit-coupler Hamiltonian. The qubit frequency is set to 4.835 GHz, while the coupler's frequency $\omega_c/(2\pi)$ varies from 4.0 GHz to 5.5 GHz. (a) Energy of eigenstates in $\{|0_q 1_c\rangle, |1_q 0_c\rangle\}$ subspace. (b) Energy of eigenstates in $\{|0_q 2_c\rangle, |1_q 1_c\rangle, |2_q 0_c\rangle\}$ subspace.

$$Z_c^\pm(t) = \frac{1}{k} \left[\pm \arcsin \sqrt{\frac{(\hbar\omega_c(t) + E_C^c)^4}{(8E_J^c E_C^c)^2} - 1} - b \right], \quad (\text{S36})$$

where E_J is the effective Josephson energy of the SQUID, d is the junction asymmetry and k and b are the effective coefficients that the magnetic flux Φ through the SQUID ring is related to Z_c by $\pi\Phi/\Phi_0 = kZ_c + b$. This waveform enables faster frequency variation of the coupler when it is far detuned from the qubit, while slowing down the change rate during proximity. Compared to ramp functions, this achieves adiabatic exchange in a shorter duration. As mentioned in the literature, experimentally we treat g as a tunable parameter to determine. And in conjunction with the coupler's start and end frequencies f_0 and f_τ , pulse duration τ and the qubit frequency, it determines the frequency trajectory. Typically, f_0 and f_τ are predetermined based on operational requirements, while the adiabaticity of the pulse can be quantified using the factor β . As for the qubit frequency in the definition of $\Delta(t)$, we change it into a tunable center frequency $\omega_{\text{center}} = 2\pi f_{\text{center}}$, and the coupler frequency is given by $\omega_c(t) = \omega_{\text{center}} + \Delta(t)$.

The waveform and the reset probability are shown in Fig. S11, S9 and S12. For resonance qubit-coupler exchange with the qubit prepared at state $|1\rangle$, we choose the qubit-coupler swap duration as 4.5 ns and coupler Z pulse amplitude 1.916 from Fig. S9(a), and then perform qubit-filter swap [Fig. S9(b)]. We verify the reset of the coupler by swapping the residual excitation back to the qubit using the same swap duration and Z pulse amplitude. Owing to the high leakage rate of the Purcell filter, the residual probability decreases steadily with time when the qubit and the filter is on resonance, which is over-damped behavior. Selecting swap duration of 70 ns and Z pulse amplitude 1.2145 is sufficient for suppressing the residual excitation on coupler below 0.5%, making it ready for being reused.

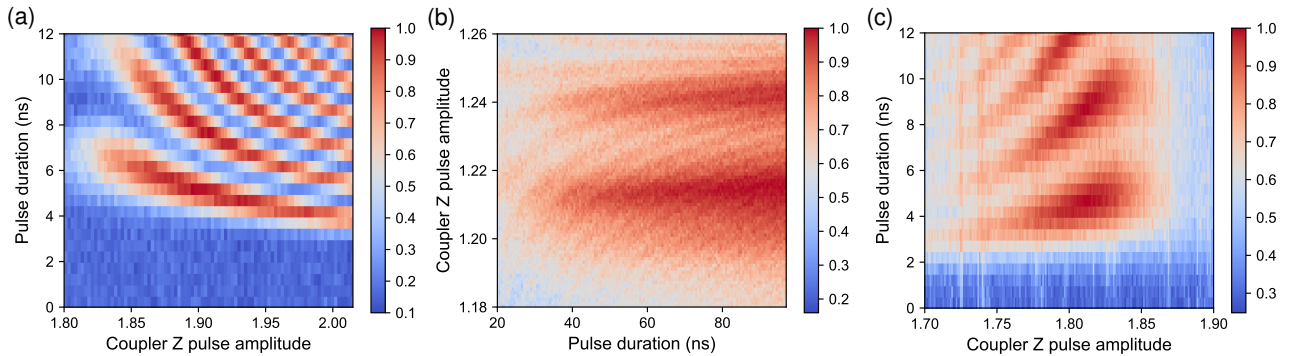


FIG. S9. Parameter scan results for resetting state $|1\rangle$ with flat square pulse. (a-b) Qubit-coupler swap and coupler-filter swap with square pulse of different coupler Z pulse amplitude and duration. (c) Qubit-coupler swap with the coupler operation point being set to the lower sweet spot.

Note that as the reset error approaches zero, the fluctuation of probability from measurement outcomes begin to dominate, necessitating increased repetition of measurements to achieve more stable results. Apart from this, we have no direct access to the excitation probability in the Purcell filter, while the reset error would accumulate if photons do not actually leak out of the filter before the next reset. To improve the accuracy and reliability of the characterization of reset error, we repeat the prepare-state-and-reset pulse sequence multiple times to enable error accumulation. And we perform scan of reset parameters with respect to the accumulation of error in average of 3000 shots to further optimize the reset fidelity. For characterizing the accumulation of error with the number of repetition, we take the average of 30000 shots for each data point, the result is presented in Fig. S14(a). The error increases and stabilized around 1.2%, the mechanism of which is explained in Appendix. VIII.

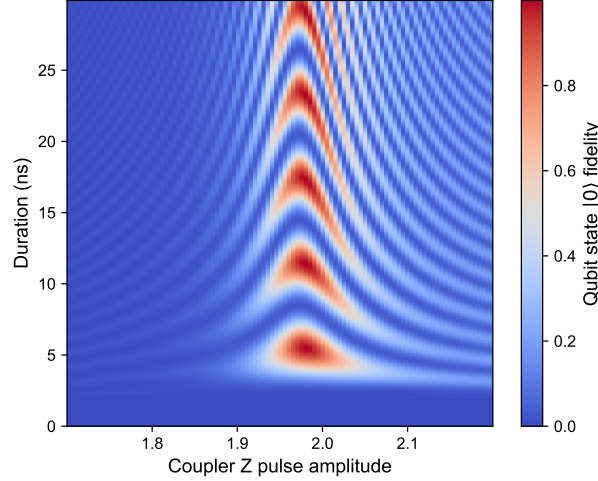


FIG. S10. Simulated reset fidelity of state $|1\rangle$ with Gaussian filtered square pulse.

If the coupler is left on its sweet spot during state preparation and readout, we find Landau-Zener-Stuckelberg (LZS) interference fringes [17] in QC swap images [Fig. S9(a)] that even when the flat stage of the Z pulse pushes the coupler to the lower sweet spot which is far off resonance with the qubit, the state probability still varies with time. As is shown in Fig. S9(c), when the idling point of the coupler is set to the lower sweet spot, the fringes of swap far below qubit frequency no longer exist, while it turns out that fringes occur far above qubit frequency, which is led by LZS interference. We can reproduce these fringes numerically by convolving analytical control pulses with a Gaussian kernel of FWHM = 1.56 ns, corresponding to a Gaussian filter function with 3 dB-attenuation bandwidth of approximately 400 MHz, to make the pulse more slow-varying, as is shown in Fig. S10, which further demonstrates that the exchange occurs when the coupler frequency crosses the qubit frequency. The features in Fig. S9(a) also partially originate from waveform distortions other than bandwidth limitations, typically exhibiting exponential-decay characteristics. Prior to acquiring data for qubit reset, we perform pulse shape calibration of the coupler's Z channel drive [18].

Though we can still perform QC swap with high fidelity for state $|1\rangle$ reset, the LZS interference effect undermines the fidelity of the adiabatic QC swap for resetting both the $|1\rangle$ and $|2\rangle$ population. If we set the coupler's operating point above the qubit frequency, and start the reset operation by first biasing the coupler frequency below the qubit frequency, then a portion of the qubit excitations would be non-adiabatically exchanged to the coupler. This results in non-negligible occupation in the dressed eigenstates overlapping predominantly with $|0_q 1_c\rangle$, $|1_q 1_c\rangle$ and $|0_q 2_c\rangle$ before performing the qubit-coupler swap. After adiabatic exchange, these eigenstates primarily overlap with $|1_q 0_c\rangle$ and $|2_q 0_q\rangle$, respectively. In other words, the excitations would be transitioned back to the qubit. Therefore, we position the coupler's operating point below the qubit frequency, so that during each reset, the coupler frequency crosses the qubit frequency only once. After the coupler-filter swap, since almost no residual excitation is left in the qubit or the coupler, biasing the coupler back to its operating point, even when it crosses the qubit frequency, this does not introduce reset error.

To avoid affecting the qubit frequency, we set the operation point of the coupler at the lower sweet spot, with Z amplitude 2.15 and frequency around 4.0 GHz. The experimental sequence maintains a $\tau_{\text{pad}} = 700$ ns interval between successive reset operations. During this interval, the coupler frequency is stabilized at the operational point while state preparation is performed using π_{10} and then π_{21} pulses with identical 150 ns durations. The state preparation commences $\tau_{\text{pre}} = 100$ ns after the completion of each reset cycle. The waveform and time intervals are depicted in Fig. S11. We set the start frequency to be 4 GHz and the end frequency 5.5 GHz. The pulse duration is set to be 30 ns. We vary the coefficient g and the center frequency f_{center} to search for optimal qubit-coupler swap parameter. For finding the coupler-filter swap parameters, we simply implement prepare-state-and-reset sequence repeated for 20 times and measure the final qubit state $|0\rangle$ probability. With coupler-filter swap parameters found, we iteratively optimize the qubit-coupler and coupler-filter swap parameters using repeated prepare-state-and-

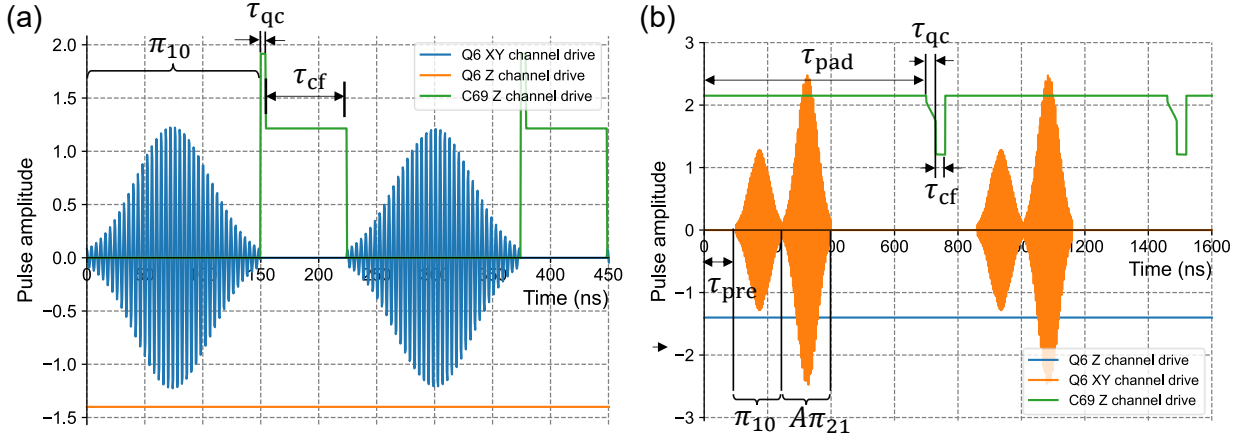


FIG. S11. The waveforms that repeat preparing state and reset for multiple times, and definition of time intervals. (a) In each cycle, the qubit state is prepared with π_{10} pulse in the XY channel and reset with qubit-coupler (QC) swap and then coupler-filter (CF) swap for square pulse duration τ_{qc} and τ_{cf} respectively. (b) In each cycle, the qubit state is prepared with π_{10} pulse and subsequent π_{21} pulse with A the amplitude scaling factor and reset with qubit-coupler swap for adiabatic pulse duration τ_{qc} and then coupler-filter swap for ramp pulse duration τ_{cf} respectively.

reset sequence. The reset fidelity scan results are shown in Fig. S12. To validate that the protocol resets both $|1\rangle$ and $|2\rangle$ well, we vary the pulse amplitude for preparing different superpositions of $|1\rangle$ and $|2\rangle$. The results show that as the proportion of the state $|2\rangle$ increases, the reset error rate exhibits only a minor increase. While it can be seen in Fig. S12(b-c) that under identical coupler-filter exchange parameters, the reset fidelity exhibits discernible discrepancies when the initial states are prepared in $|1\rangle$ versus $(|1\rangle + |2\rangle)/\sqrt{2}$. A longer swap duration is required to achieve low residual error rate when it involves state $|2\rangle$ occupation. We find optimal parameters $f_{\text{center}} = 4.86$ GHz, $g/(2\pi) = 0.605$ MHz, $\tau_{qc} = 30$ ns, $\tau_{cf} = 170$ ns, $Z_c^{(cf)} = 1.209$ and the slope of the coupler-filter swap pulse $m_{cf} = -0.00016$ /ns. The scatter plot of raw IQ data points used for calculating the reset fidelity is presented in Fig. S7.

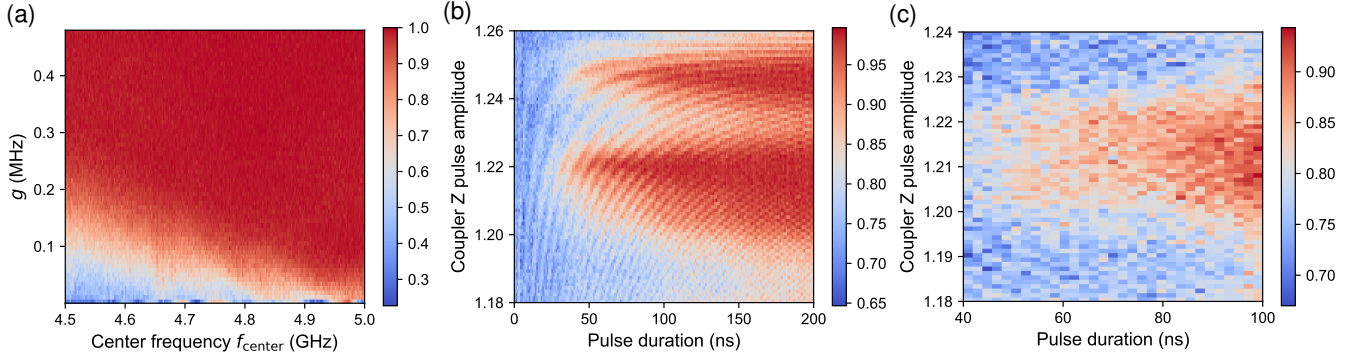


FIG. S12. Parameter scan of Q6 state $|0\rangle$ probability for resetting both $|1\rangle$ and $|2\rangle$ state with adiabatic pulse. (a) Adiabatic qubit-coupler swap with different g and center frequency f_{center} . (b) Coupler-filter swap with state preparation and reset process repeated for 20 times. Each state preparation is performed by applying a π_{10} pulse. (c) Coupler-filter swap with state preparation and reset process repeated for 20 times, while each state preparation is performed by applying a π_{10} pulse and subsequently a $\pi_{21}/2$ pulse.

We numerically illustrate how LZS interference affect the reset fidelity by convolving the Z pulse with Gaussian kernels of different standard deviations [Fig. S13]. Using the same pulse parameters while setting the coupler's operating point below and above qubit frequency respectively, it's found that in the former case, the reset error rate remains unaffected by the filter function. This reset protocol demonstrates remarkable robustness over waveform distortion and bandwidth limitations. In the latter case, however, as the waveform evolves more gradually, the reset error rate exhibits a substantial increase. By simulating the coupler biasing from its upper sweet spot to lower sweet spot, while staying at the lower sweet spot subsequently, it's found that the excitation transfers from the qubit to the coupler during the process.

The high leakage rate enables rapid reset and reuse of the Purcell filter, even if it is shared across multiple couplers for

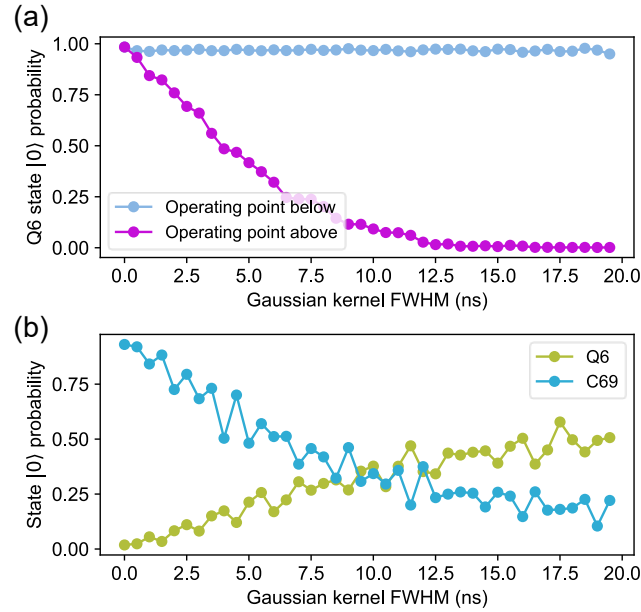


FIG. S13. The effect of LZS interference on reset fidelity. (a) Comparison of reset fidelity with the coupler's operating point below and above qubit frequency. (b) The excitation of Q6 transfers to C69 during the process of biasing the coupler's frequency below qubit frequency from above, contributing to more reset error as the Gaussian kernel width increases.

performing reset operation. The coupler-filter swap is over-damped, and higher reset fidelity can be reached by allowing slightly longer swap duration [Fig. S15], which is in contrast to the under-damped behavior that can occur when using qubit-resonator swap, where the coupler excitation can not be transferred completely at the minimum points of each swap circle due to the dissipation and we have discrete time points to choose from [Fig. S14(b)]. With this, the coupler-filter swap is theoretically more efficient since the leakage rate of the resonator is small, which should match 2χ while χ is designed to be small to protect the qubit from decoherence, and using coupler-resonator swap would potentially introduce larger qubit dephasing rate over a significant duration.

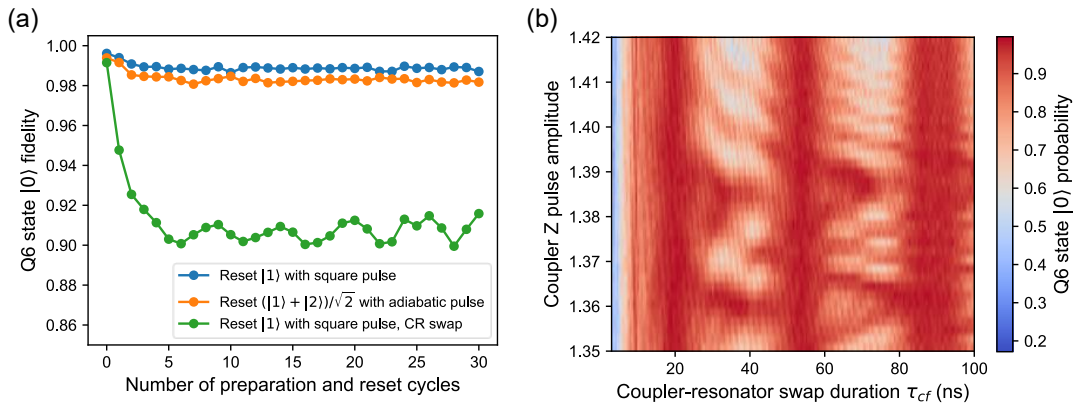


FIG. S14. (a) Reset error accumulation with the number of state preparation and reset cycles. The qubit states are reset with square pulse and CF swap, adiabatic pulse and CF swap, and square pulse but CR (coupler - readout resonator) swap, where the readout filter Z pulse amplitude is set to 1.36 during the swap. (b) Coupler reset fidelity with respect to qubit with 1 reset cycle. The coupler is reset with the resonator, and the residual excitation is measured by swapping back the excitation to the qubit. The filter Z pulse amplitude is set to 1.5 to reach high resonator leakage rate.

To validate the scalability of the coupler-filter coupling architecture, we numerically simulate the situation where multiple couplers simultaneously perform resonant exchange with a common Purcell filter, the result of which is shown in Fig. S16. The couplers are assumed to be identical. They are all prepared in state $|1\rangle$ and then set to be resonant with the filter. As the number of number of couplers increases, the reset process of each coupler becomes faster, due to the fact that the qubit excitations are

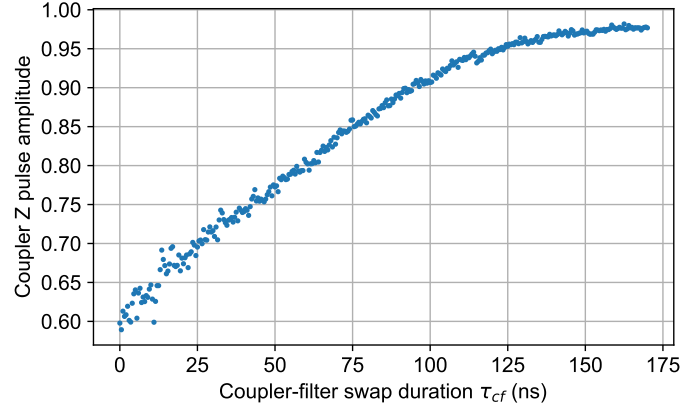


FIG. S15. The reset fidelity after 20 state-preparation-and-reset cycles increases with the coupler-filter swap duration monotonically.

swapped to higher energy levels of the Purcell filter with low anharmonicity, where the corresponding state decay rate is larger. Therefore, as the excitations accumulate to higher levels, each excitation obtains a larger average decay rate.

However, a more common situation is that only part of the qubits are excited or the qubit states are in superpositions of $|0\rangle$ and the excited states. Numerical results show that when the couplers are partially excited, the exchange will reach a stage where the excitations will persist in the couplers without dissipation [Fig. S17]. The initial states are prepared in $|1_1 0_2 0_3 0_4 0_5 0_6 0_f\rangle$, $|1_1 1_2 0_3 0_4 0_5 0_6 0_f\rangle$, $|1_1 1_2 1_3 0_4 0_5 0_6 0_f\rangle$, $|1_1 1_2 1_3 1_4 0_5 0_6 0_f\rangle$, $|1_1 1_2 1_3 1_4 1_5 0_6 0_f\rangle$ and $|1_1 1_2 1_3 1_4 1_5 1_6 0_f\rangle$ respectively. To simplify the notations, we denote $n_{|1\rangle}$ as the number of couplers that are prepared in state $|0\rangle$ and $n_{|0\rangle}$ as the number of couplers prepared in state $|1\rangle$. It's found that the qubits prepared in state $|0\rangle$ undergo excitation during the exchange, and the more qubits prepared in state $|1\rangle$, the higher population of the prepared-state- $|0\rangle$ qubit's excited states when equilibrium, while the more excited state population of the qubits prepared in state $|1\rangle$ dissipate out. This phenomena can be explained by the fact that the Lindbladian superoperator \mathcal{L} of the system has eigenstates whose corresponding eigenvalues contains approximately zero image part and there is no excited state population of the filter. When the initial state is prepared to overlap with them, these parts do not dissipate. It poses a challenge for simultaneously resetting all of the couplers. Future research may explore frequency modulation techniques to prevent the emergence of these eigenstates in quantum systems.

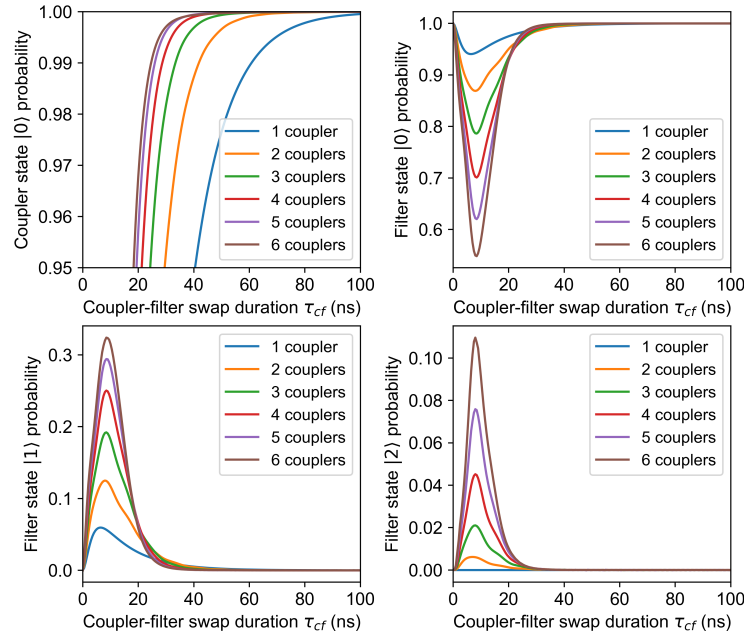


FIG. S16. Different numbers of couplers performing coupler-filter swap with a common Purcell filter simultaneously. The couplers are designed to be identical and the initial states of the couplers are all prepared to be $|1\rangle$.

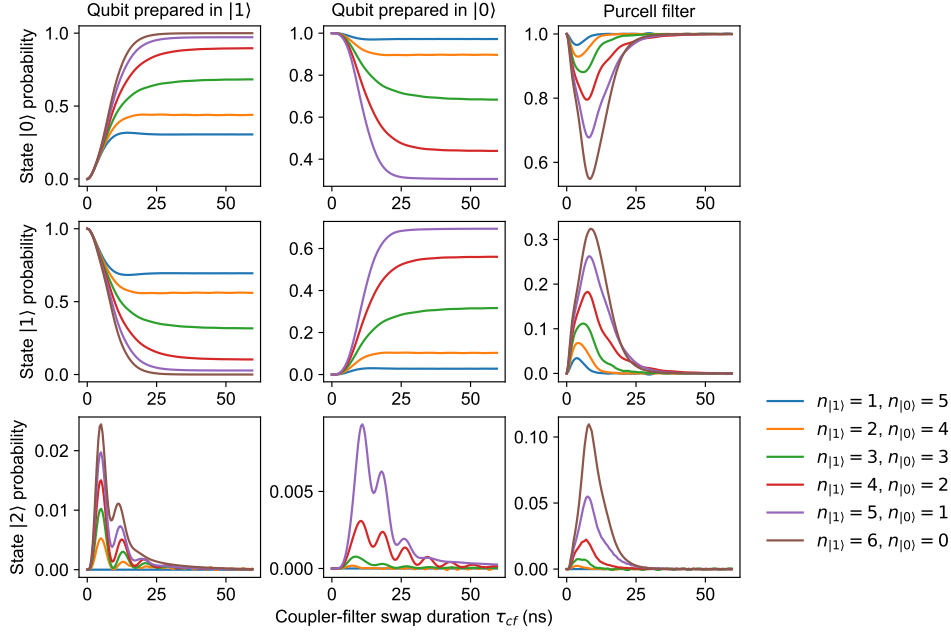


FIG. S17. 6 couplers simultaneously swap with a common Purcell filter with different number of qubits prepared in state $|1\rangle$ while others prepared in $|0\rangle$.

VIII. ANALYSIS OF RESET ERROR ACCUMULATION

We posit that the error accumulation during multiple reset operations primarily evaluates the effectiveness of the decay of the Purcell filter. This is because if the coupler-qubit exchange achieves unconditional reset, even imperfect qubit reset would at most introduce errors in subsequent state preparation, potentially resulting in lower population of $|2\rangle$ and $|1\rangle$ states compared to scenarios without reset errors. Conversely, in the coupler-qubit exchange process, incomplete coupler reset would lead to residual excitations being transferred back to the qubit. With the residual excitation accumulates in the Purcell filter, the residual excitation of the coupler after the coupler-filter swap increases, which finally induces accumulation in qubit reset error.

We reproduce the phenomena numerically and further illustrate this mechanism, as shown in Fig. S18. The coupler-filter swap duration is intentionally reduce to 70ns to introduce larger reset error of the coupler, and the filter dissipation during qubit state preparation is omitted. After the first preparation and reset operation, even though the qubit is reset with high fidelity with adiabatic qubit-coupler swap, the coupler's residual excitation is significant, which is swapped backed to the qubit in the next reset cycle. As the filter does not completely dissipate to thermal equilibrium, the coupler-filter swap in the second reset cycle has larger coupler reset error. The residual excitation of the coupler is progressively swapped to the qubit, thus leading to accumulation of the qubit's reset error. While the state preparation introduces more excitation, the amount of excitation that coupler exchanges to the filter increase due to larger excited state occupation and therefore larger exchange rate. This two mechanism competes and finally lead to equilibrium, resulting in stable reset error in the following reset cycles.

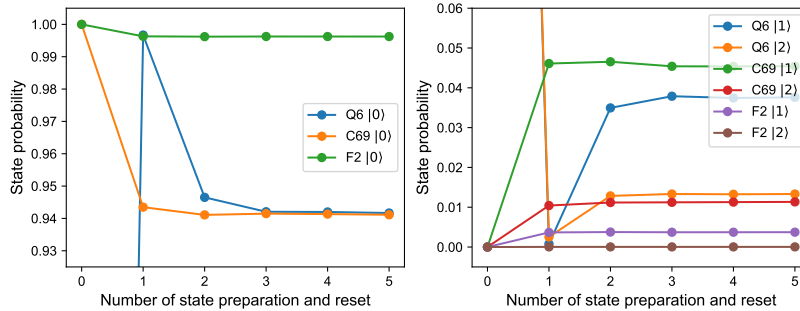


FIG. S18. Numerical demonstration of reset error accumulation due to imperfect coupler-filter swap.

The accumulation of reset error can be reduced if we perform multiple reset after each state preparation, as is presented in the main text and can also be reduced predominantly by performing longer coupler-resonator swap [Fig. S15]. We can make a trade off between reset time and reset fidelity, depending on experimental requirements.

-
- [1] Y. Sunada, K. Yuki, Z. Wang, T. Miyamura, J. Ilves, K. Matsuura, P. A. Spring, S. Tamate, S. Kono, and Y. Nakamura, Photon-Noise-Tolerant Dispersive Readout of a Superconducting Qubit Using a Nonlinear Purcell Filter, *PRX Quantum* **5**, 010307 (2024).
 - [2] Z.-X. Man, Y.-J. Xia, and R. Lo Franco, Harnessing non-Markovian quantum memory by environmental coupling, *Phys. Rev. A* **92**, 012315 (2015).
 - [3] D. M. Pozar, *Microwave engineering* (Microwave engineering, 2004).
 - [4] P. Krantz, M. Kjaergaard, F. Yan, T. P. Orlando, S. Gustavsson, and W. D. Oliver, A quantum engineer's guide to superconducting qubits, *Appl. Phys. Rev.* **6**, 021318 (2019).
 - [5] A. Blais, A. L. Grimsmo, S. M. Girvin, and A. Wallraff, Circuit quantum electrodynamics, *Rev. Mod. Phys.* **93**, 025005 (2021).
 - [6] E. A. Sete, J. M. Martinis, and A. N. Korotkov, Quantum theory of a bandpass Purcell filter for qubit readout, *Phys. Rev. A* **92**, 012325 (2015).
 - [7] C. C. Bultink, B. Tarasinski, N. Haandbæk, S. Poletto, N. Haider, D. J. Michalak, A. Bruno, and L. DiCarlo, General method for extracting the quantum efficiency of dispersive qubit readout in circuit QED, *Appl. Phys. Lett.* **112**, 092601 (2018).
 - [8] J. Koch, T. M. Yu, J. Gambetta, A. A. Houck, D. I. Schuster, J. Majer, A. Blais, M. H. Devoret, S. M. Girvin, and R. J. Schoelkopf, Charge-insensitive qubit design derived from the Cooper pair box, *Phys. Rev. A* **76**, 042319 (2007).
 - [9] S. S. Elder, C. S. Wang, P. Reinhold, C. T. Hann, K. S. Chou, B. J. Lester, S. Rosenblum, L. Frunzio, L. Jiang, and R. J. Schoelkopf, High-Fidelity Measurement of Qubits Encoded in Multilevel Superconducting Circuits, *Phys. Rev. X* **10**, 011001 (2020).
 - [10] G.-H. Liang, X.-H. Song, C.-L. Deng, X.-Y. Gu, Y. Yan, Z.-Y. Mei, S.-L. Zhao, Y.-Z. Bu, Y.-X. Xiao, Y.-H. Yu, M.-C. Wang, T. Liu, Y.-H. Shi, H. Zhang, X. Li, L. Li, J.-Z. Wang, Y. Tian, S.-P. Zhao, K. Xu, H. Fan, Z.-C. Xiang, and D.-N. Zheng, Tunable-coupling architectures with capacitively connecting pads for large-scale superconducting multiqubit processors, *Phys. Rev. Appl.* **20**, 044028 (2023).
 - [11] D. Sank, A. Opremcak, A. Bengtsson, M. Khezri, Z. Chen, O. Naaman, and A. Korotkov, System Characterization of Dispersive Readout in Superconducting Qubits (2024), [arXiv:2402.00413 \[quant-ph\]](https://arxiv.org/abs/2402.00413).
 - [12] R. Vijay, M. H. Devoret, and I. Siddiqi, Invited Review Article: The Josephson bifurcation amplifier, *Rev. Sci. Instrum.* **80**, 111101 (2009).
 - [13] J. Choi, H. Hwang, and E. Kim, Measurement-induced bistability in the excited state of a transmon, *Phys. Rev. Appl.* **22**, 054069 (2024).
 - [14] T. Akiba, S. Sano, T. Yanase, T. Ohta, and M. Koyama, Optuna: A Next-generation Hyperparameter Optimization Framework, in *Proceedings of the 25th ACM SIGKDD International Conference on Knowledge Discovery & Data Mining*, KDD '19 (Association for Computing Machinery, New York, NY, USA, 2019) p. 2623–2631.
 - [15] H. Yan, X. Wu, A. Lingenfelter, Y. J. Joshi, G. Andersson, C. R. Conner, M.-H. Chou, J. Grebel, J. M. Miller, R. G. Povey, H. Qiao, A. A. Clerk, and A. N. Cleland, Broadband bandpass Purcell filter for circuit quantum electrodynamics, *Appl. Phys. Lett.* **123**, 134001 (2023).
 - [16] L. Chen, S. P. Fors, Z. Yan, A. Ali, T. Abad, A. Osman, E. Moschandreou, B. Lienhard, S. Kosen, H.-X. Li, D. Shiri, T. Liu, S. Hill, A.-A. Amin, R. Rehammar, M. Dahiya, A. Nylander, M. Rommel, A. F. Roudsari, M. Caputo, G. Leif, J. Govenius, M. Dobsicek, M. F. Giannelli, A. F. Kockum, J. Bylander, and G. Tancredi, Fast unconditional reset and leakage reduction in fixed-frequency transmon qubits (2024), [arXiv:2409.16748 \[quant-ph\]](https://arxiv.org/abs/2409.16748).
 - [17] G. Kim, A. Butler, V. S. Ferreira, X. S. Zhang, A. Hadley, E. Kim, and O. Painter, Fast unconditional reset and leakage reduction of a tunable superconducting qubit via an engineered dissipative bath, *Phys. Rev. Appl.*, (2025).
 - [18] T.-M. Li, J.-C. Zhang, B.-J. Chen, K. Huang, H.-T. Liu, Y.-X. Xiao, C.-L. Deng, G.-H. Liang, C.-T. Chen, Y. Liu, H. Li, Z.-T. Bao, K. Zhao, Y. Xu, L. Li, Y. He, Z.-H. Liu, Y.-H. Yu, S.-Y. Zhou, Y.-J. Liu, X. Song, D. Zheng, Z. Xiang, Y.-H. Shi, K. Xu, and H. Fan, High-precision pulse calibration of tunable couplers for high-fidelity two-qubit gates in superconducting quantum processors, *Phys. Rev. Appl.* **23**, 024059 (2025).